Materials Advances

Accepted Manuscript

This article can be cited before page numbers have been issued, to do this please use: A. Chakravorty, S. Das, A. Appu Mini, S. Awasthi, S. K. Pandey and V. Raghavan, *Mater. Adv.*, 2025, DOI: 10.1039/D4MA01245C.

ROYAL SOCIETY
OF CHEMISTRY

rsc.li/materials-advances

View Article Online
DOI: 10.1039/D4MA01245C

MXene-derived Potassium Titanate Nanoribbons Decorated Electrode Architecture for Detection of Ciprofloxacin: A Multipurpose Sensing Platform Development

[a]Arghya Chakravorty†, [a]Sudip Das†, [a]Aarcha Appu Mini†, [b]Shikha Awasthi, [c]Sarvesh Kumar Pandey*, [a]Vimala Raghavan*

*Corresponding Author - vimala.r@vit.ac.in (VR); sarvesh@manit.ac.in (SKP)

[a]Centre for Nanotechnology Research, Vellore Institute of Technology, Vellore, Tamil Nadu, 632014 – India.

[b]Department of Chemistry, Manipal University Jaipur, Jaipur, Rajasthan 303 007 – India.

[c]Department of Chemistry, Maulana Azad National Institute of Technology Bhopal, Bhopal, Madhya Pradesh, 462 003 – India.

†Authors contributed equally to this manuscript.

Abstract

Recent studies have highlighted the promise of MXene-derived titanate nanoribbons (KTNR) as electrode materials for electrochemical sensing applications. This work investigates the electrochemical activity of potassium titanate nanoribbons synthesized from MXene for the development of a voltammetric sensor for ciprofloxacin detection. The sensor offers a sustainable approach for ciprofloxacin quantification, addressing critical needs in food safety, environmental monitoring, and healthcare diagnostics, ultimately contributing to the United Nations' Sustainable Development Goals by mitigating antimicrobial resistance and supporting the One Health initiative. To initiate the experiments, the structural, stability/energetics, and electronic features of two dimer complexes, KTNR/ciprofloxacin and MXene/ciprofloxacin, have been computationally inspected using two in-silico tools, and some important electronic parameters such as binding energy, HOMO-LUMO gap, dipole moment show that the former one (KTNR) is significantly more sensitive than the MXene with the ciprofloxacin. 2D Ti3C2 MXene served as the precursor for the synthesis of potassium titanate nanoribbons. X-ray diffraction (XRD), field emission scanning electron microscopy (FESEM), high-resolution transmission electron microscopy (HRTEM), selected area electron diffraction (SAED), elemental mapping, and energy-dispersive X-ray spectroscopy (EDX) techniques were employed to confirm the crystallinity, surface morphology, and layered structure of the synthesized nanoribbons. The electrochemical and sensing properties of the materials were further evaluated using cyclic voltammetry (CV), differential pulse voltammetry (DPV), and electrochemical impedance spectroscopy (EIS). Subsequently, the nanoribbons were deposited onto a glassy carbon electrode (GCE) surface. The electro-oxidation behaviour of ciprofloxacin was then investigated using CV, DPV, and square wave voltammetry (SWV) in an optimized 0.1 M phosphate buffer solution (pH 8). The developed sensor exhibited a remarkable linear detection range of 0.6 µM (≈ 0.03 µg mL-1) to 147.2 µM (≈ 7.18 µg mL-1) for ciprofloxacin. Additionally, the limit of detection (LOD) achieved was 0.07, 0.0608, and 0.0264 µM for CV, DPV, and SWV, respectively. Notably, the electrodes demonstrated excellent selectivity towards ciprofloxacin detection in complex matrices, including marine water, river water, agricultural soil, organic fertilizer, milk, honey, poultry eggs, and simulated body fluids.

Keywords: MXene derivative, Potassium titanate nanoribbons, electrochemical sensor, ciprofloxacin, healthcare monitoring, food and environmental safety.

1. Introduction

Ciprofloxacin is a double-edged sword. While it's a crucial antibiotic, its overuse and presence in the environment and food contribute significantly to the global antimicrobial resistance (AMR) crisis. It's an antibiotic with the ability to inhibit bacterial DNA gyrase. It is used to treat humans against a variety of bacterial infections, including urinary tract infections, respiratory tract infections, skin infections, and certain sexually transmitted diseases. It is also evident, that like the other broad-spectrum fluoroquinolone group of antibiotics, ciprofloxacin is also predominantly effective in growth promotion and treating several deadly infections in animal husbandry, including cattle farms, poultry farms, fisheries, and apiculture. However, overuse and misuse of antibiotics like ciprofloxacin are responsible for the development of (AMR). The relationship between AMR and ciprofloxacin lies in the selective pressure exerted by the widespread use of this antibiotic. When bacteria are exposed to ciprofloxacin, some of them may possess genetic mutations or acquire resistance genes that enable them to survive the antibiotic's effects. Through natural selection, these resistant bacteria can then proliferate and spread, leading to the emergence of ciprofloxacin-resistant strains. Ciprofloxacin-resistant bacteria pose a significant challenge. Infections caused by them become more difficult to treat, requiring stronger antibiotics, alternative therapies, and precision dosing through therapeutic drug monitoring. This can lead to longer hospital stays, increased healthcare costs, and even higher mortality rates [1–9].

The WHO reports show variations, but ciprofloxacin resistance in bacteria like *E. coli* and *Klebsiella pneumonia* can range from 4% to 93% across countries [10]. This highlights the growing global problem. Traces of ciprofloxacin can end up in rivers and marines through wastewater. Studies suggest even low concentrations of ciprofloxacin in the environment can promote AMR in *E. coli* present there. In brief, it can affect the whole marine and freshwater ecosystem. Through the food chain, the resistant bacteria and the antibiotic residues enter to human system, even animal-based foods like eggs, meat, milk, and honey also contain ciprofloxacin residues. This further significantly complicates the same global challenges [11–16].

As a diagnostic analytical approach to measuring the concentration of different bio-analytes [17,18]and antibiotics [19–23], specifically ciprofloxacin, several versatile and efficient analytical tools have been developed like ultra-high performance liquid chromatography-mass spectrometry, quadrupole time of flight mass-spectroscopy, liquid chromatography-mass spectrometry, which are recognized as a gold standard tool to measure ciprofloxacin concentration in food (viz. milk, eggs, meat, fish, honey), environmental (wastewater, river and marine water, agricultural soils, organic fertilizers), and biomedical (viz. body fluids like blood serum, urine) samples [24]. Though these tools are highly reliable, sensitive, and efficient in measuring a wide concentration range; due to the high expenditure, and maintenance these techniques are unable to be installed in resource-limited settings. In this context, the development of alternative versatile technology is highly required to measure ciprofloxacin concentration in various real matrices. Thus, a cost-effective electrode material has been reported **(as shown in Scheme. 1)** by using MXene-derived potassium titanate nanoribbons. Here, the electro-catalysis of ciprofloxacin has been demonstrated as a fundamental mechanistic approach.

In our study, we have already explored the potential of novel nanoribbons derived from MXene (titanium carbide) as an electrochemical sensing platform to provide food safety. These nanoribbons possess several unique characteristics that make them ideal for this application. Firstly, they possess an intrinsic ability to amplify signals within the material itself, eliminating the need for separate amplifiers. They exhibit exceptional stability over the time, ensuring reliable performance, and demonstrated high sensitivity toward analytes crucial for food safety, as reported by Mini and Raghavan (2024) [25]. The specific structure of these nanoribbons, with their layered morphology and abundant hydroxyl groups on the surface, provides a large

View Article Online
DOI: 10.1039/D4MA01245C

surface area, making them well-suited for ciprofloxacin detection. In addition to that, the presence of polar bonds in ciprofloxacin is due to the electronegativity difference between the atoms involved in its chemical structure. Here, the presence of polar bonds leads to an uneven distribution of electron density within the molecule, resulting in regions of partial positive and partial negative charge. This polarity allows ciprofloxacin to interact with other polar molecules or ions, which is important for its mechanism of action as an antibiotic and for its solubility in aqueous environments, as well as facilitating its electrocatalytic behaviour [1–3,25–33]. Interestingly, our research shows that ciprofloxacin, a molecule with polarity, triggers a decrease in the resistance of these nanoribbons during the catalytic events. This finding contributes to a deeper understanding of electrochemical sensing mechanisms that exploit proton conduction. Our work highlights the promise of this electrocatalytic approach for achieving ultra-low limits of ciprofloxacin detection with exceptional selectivity even in different real and complex matrices. These are again related to ciprofloxacin sensing for food and environmental safety along with biomedical purposes like therapeutic drug monitoring (TDM).

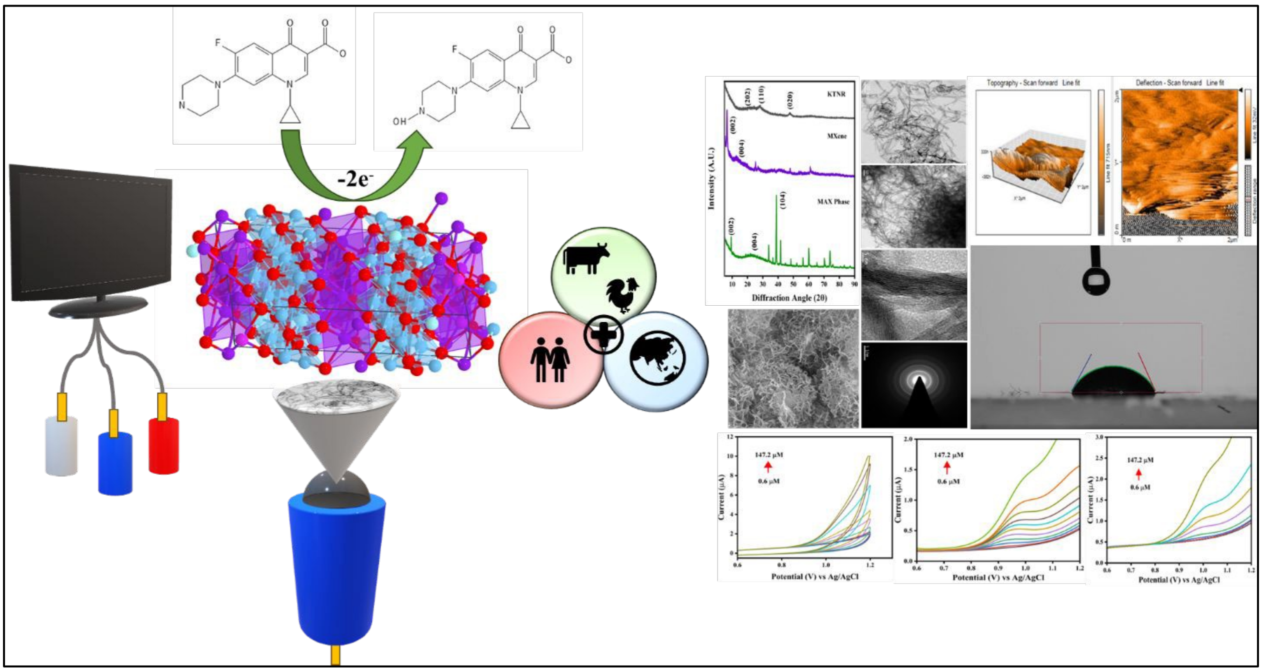

Scheme 1. Schematic illustration of KTNR fabricated multi-purpose electrochemical sensor for ciprofloxacin detection.

2. Experimental Section

2.1. Computational Methodology

Computational tools have imperative role in understanding and unraveling the quantum (atomic and molecular) level features. Due to the large size of both dimer complexes (KTNR-ciprofloxacin and MXene-ciprofloxacin) consisting of a large number of heavy metals (like K and Ti in the KTNR and Ti in the MXene), the calculations demanded high computational costing. The optimization and frequency calculations have been executed using the semiempirical approach however, an ab-initio, Hartree-Fock (HF) functional and 6-31G basis set have been used for single point calculations for the F, O, N, C, N, H, and K atoms and SDD for the Ti (transition metal) atom. Since, by keeping the experimental facets, this report discusses some important geometry, energetic/stability, and electronic parameters using molecular modelling and electronic feature analyses in the framework of semiempirical and ab-initio modeling approaches. All quantum chemical calculations have been executed using the immensely used Gaussian 09 electronic structure calculations package [34]

2.2. Reagents and Equipments

Ciprofloxacin (≥99.0%; pharmaceutical secondary standard), enrofloxacin (≥99.0%), norfloxacin (≥98%, TLC), ofloxacin (≥98%; Pharmaceutical Secondary Standard), nafion, uric acid (≥99%, crystalline), urea (99.0-100.5%, ACS reagent), dopamine hydrochloride (≥98%; Pharmaceutical Secondary Standard), diclofenac sodium (≥98%; Pharmaceutical Secondary Standard), D-glucose (≥99.5% - GC, BioXtra), 48% hydrofluoric acid (≥99.99% trace metals basis), Titanium aluminium carbide MAX phase (910775; ≥90%, ≤40 µm particle size), and ascorbic acid (≥98%; Pharmaceutical Secondary Standard) were purchased from Sigma Aldrich, India. Other supporting reagents were procured from SD Fine Chemicals, Mumbai, India; Avra Synthesis Pvt. Ltd. India. All the chemicals were used without any further purification. 0.1 M NaH_2PO_4 and 0.1 M Na_2HPO_4 were used to prepare a phosphate buffer solution with the required pH.

Powder X-ray diffraction (XRD) (Bruker D8 Advance, Panalytical X Pert3, Germany, Netherlands), field emission scanning electron microscopy (FE-SEM), and energy-dispersive X-ray analysis (EDAX) (Thermo Fisher, FEI QUANTA 250 FEG), high-resolution transmission electron Microscope (HR-TEM) and selected area electron diffraction (SAED) (FEI –TECNAI, G2-20 TWIN - Operating voltage 200 kV) have been used to characterize materials and provided the high-resolution images of the internal structures of the active electrode material, including details of its crystal lattice, atomic arrangements, and defects down to the atomic level. The CHI 660C electrochemical workstation has been used for all

View Article Online
DOI: 10.1039/D4MA01245C

electrochemical measurements including cyclic voltammetry (CV), differential pulse voltammetry (DPV), square wave voltammetry (SWV), and electrochemical impedance spectroscopy (EIS). The fabricated electrode surfaces were characterized by the atomic force microscope (Nanosurf AFM, Nanosurf, Switzerland), surface profilometer (Marsurf XR20, Mahr), wettability test (contact angle metre HO-IAD-CAM-01A, HOLMARC). Throughout the experiments, 0.3 μm alumina slurry was used to polish the active surface of glassy carbon electrodes (GCE) to make it used as a working electrode, while Ag/AgCl (3 M KCl) and platinum wire performed as a reference and counted electrode in a three-electrode system.

2.3. Synthesis of MXene and MXene-derived Potassium Titanate Nanoribbons (KTNR)

MXene was synthesized by the priorly optimized HF etching of the MAX phase and delaminated by DMSO [35,36]. Potassium titanate nanoribbons (KTNR) were synthesized via a well-established methodology employing MXene as the precursor [37]. In the initial stage, 100 mg of MXene was incorporated into a mixture comprised of 30 mL of 1 M KOH solution and 0.68 mL of 30% H_2O_2. This resultant mixture was subsequently transferred to a 50 mL Teflon-lined stainless-steel autoclave. The autoclave underwent hydrothermal treatment at 150°C for a duration of 16 hours, facilitating the transformation of MXene into KTNR. Following natural cooling of the autoclave to ambient temperature, the uppermost layer, containing a white suspension, was isolated using vacuum filtration. The obtained KTNR sample was then subjected to rigorous washing with deionized (DI) water and ethanol to eliminate any residual byproducts from the reaction. Finally, the purified KTNR was desiccated in an oven at 60°C for 12 hours to remove any remaining solvent molecules [25,38,39].

2.4. Preparation of complex matrices

The performance of the fabricated KTNR electrochemical sensor was evaluated in various real-world matrices with clinical significance for trace ciprofloxacin detection. These matrices included simulated body fluid (SBF) to mimic physiological conditions and animal-derived food samples (honey, milk, and eggs) obtained from local markets in Kerala and Tamil Nadu, India. Environmental water samples were also tested, encompassing river water (Ganga) and marine water (Bay of Bengal) collected from West Bengal, India. Additionally, agricultural soil and organic fertilizer were analyzed, and sourced from local agricultural fields and farms in Vellore, India.

View Article Online
DOI: 10.1039/D4MA01245C

A standardized sample preparation procedure was employed for food and environmental samples. Briefly, samples were homogenized and filtered using a 0.22 μm nylon filter. Subsequently, they underwent a 10-fold dilution with phosphate buffer (pH 8) before being spiked with ciprofloxacin to achieve a concentration (including 15 μM). For agricultural samples, 1 g of the solid material was ultrasonicated in 10 ml of deionized (DI) water, followed by centrifugation at 3000 rpm for 10 minutes. The resulting supernatant was collected, filtered with a 0.22 μm nylon filter, diluted 10-fold with phosphate buffer (pH 8), and spiked with ciprofloxacin to reach a final concentration of 15 μM.

3. Results and Discussions

3.1. Computational Studies

Comprehensive computational studies on the structural, stability/energetic, and electronic features of a variety of molecular systems can be viewed in the reports along with biomaterials [40,41]. All optimized structures (monomer constituents and dimer complexes) are shown in **Figure 1**. Here in this report, a few chosen structural/geometrical parameters (particularly, the bond distance between the atoms of two interacting monomer constituents) had been calculated for both dimer complexes (KTNR/Ciprofloxacin and MXene/Ciprofloxacin) which are shown in **Figure 1**. Having a look into the first case as the KTNR/Ciprofloxacin dimer complex, a total of five nonbonding interactions between two components (KTNR and Ciprofloxacin) were shown in the dotted line. The bond lengths of the two K---N (3.040 Å and 2.919 Å) and three weak C-H---O (2.120 Å, 2.162 Å, and 2.489 Å) H-bonding interactions involved in the KTNR/Ciprofloxacin dimer complex can be seen in **Figure 1**. However, only two metal-nonmetal interactions (Ti---O) could be discerned for the MXene-Ciprofloxacin dimer complex whose bond lengths are 2.029 Å and 2.189 Å. The structural parameters appeared to indicate that the former one (KTNR/Ciprofloxacin) could be structurally more favorable than the latter one (MXene/Ciprofloxacin).

View Article Online
DOI: 10.1039/D4MA01245C

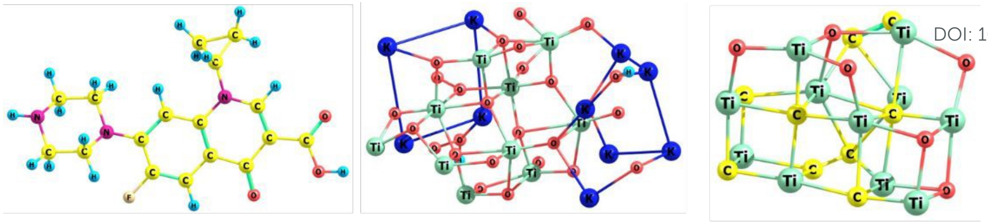
Ciprofloxacin KTNR Mxene

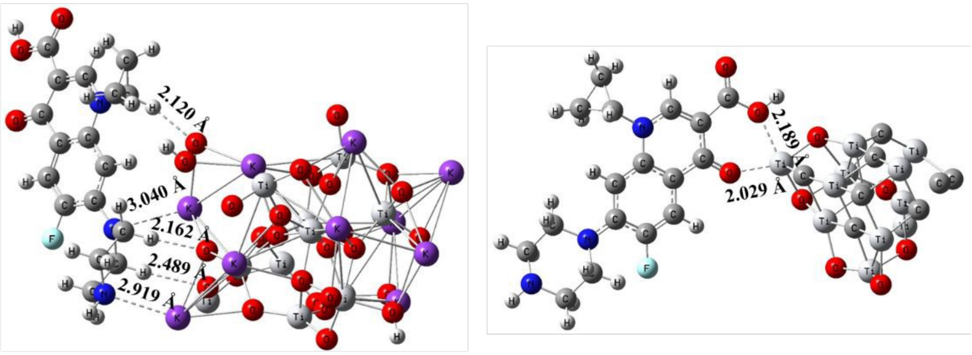

KTNR-Ciprofloxacin MXene-Ciprofloxacin

Figure 1. Optimized Structures of the Monomer Constituents (ciprofloxacin, KTNR, and MXene) and Dimer Complexes (KTNR-ciprofloxacin and MXene-ciprofloxacin).

In order to inspect the sensitivity/binding feature (also, linked to the structural features) of both dimer complexes (KTNR-ciprofloxacin and MXene-ciprofloxacin), the binding energies (BEs) had been analyzed which can be seen in **Table 1** [42]. The semiempirical approach (PM6) showed that the BE of the KTNR-ciprofloxacin complex (254.6 kcal/mol) was found to be five times greater than that of the MXene-ciprofloxacin complex (-50.6 kcal/mol). Very importantly and notably, the HF/6-31G method also showed that the BE of the former one (-501.8 kcal/mol) was found to be 5.4 times stronger than that of the latter one (-92.7 kcal/mol). Such BE-based findings clearly demonstrated that the KTNR was more sensitive than the MXene with the ciprofloxacin which also supports to the experiment-based outcomes in the later part of research.

Table 1. Some Important and Chosen Electronic Parameters of the KTNR-Ciprofloxacin and MXene-Ciprofloxacin Dimer Complexes

System	KTNR-ciprofloxacin	MXene-ciprofloxacin
BE (PM6)	-254.6 kcal/mol	-50.6 kcal/mol
BE [HF (SP)/6-31G]	-501.8 kcal/mol	-92.7 kcal/mol

View Article Online
DOI: 10.1039/D4MA01245C

HOMO	-5.480	-5.818
LUMO	-0.610	0.250
E_{Gap}	4.87	5.568
Dipole Moment	32.1	23.8
Natural Charge (e)	KTNR (0.023e) and ciprofloxacin (-0.023e)	MXene (0.415e) and ciprofloxacin (-0.415e)

Moreover, as the Frontier molecular orbitals (FMOs), like highest occupied molecular (HOMO) and lowest unoccupied molecular orbital (LUMO), and the associated HOMO-LUMO energy gap (E_{Gap}) being useful diagnostics of showing the sensitivity/reactivity features, such parameters (HOMO, LUMO, and E_{Gap}) had been probed. A system having low E_{Gap} value showed that the system was more sensitive/chemically reactive. The E_{Gap} of both KTNR-ciprofloxacin and MXene-ciprofloxacin complexes had been detected as 4.87 eV and 5.568 eV, respectively which further validated that the former one was more sensitive than the latter one. Interestingly, a system consisting of a large dipole moment (DM) indicated it's more sensitivity/chemical reactivity. Here, in this report the DMs of the KTNR- and MXene-based complexes were computed as 32.1 Debye (D) and 23.8 D which also assured about the more sensitivity of the former one. Additionally, the natural charges on each monomer constituents of both dimer complexes have been examined and it was found that the ciprofloxacin consisted of negative charge (-0.023e) and KTNR had a positive charge (+0.023e). A similar trend can be viewed in the case of the MXene-ciprofloxacin complex where a significant large charge difference (MXene: +0.415e and ciprofloxacin: -0.415e) was therein. Such findings illustrate that the charge transfer (CT) took place from KTNR/MXene to the ciprofloxacin component.

View Article Online
DOI: 10.1039/D4MA01245C

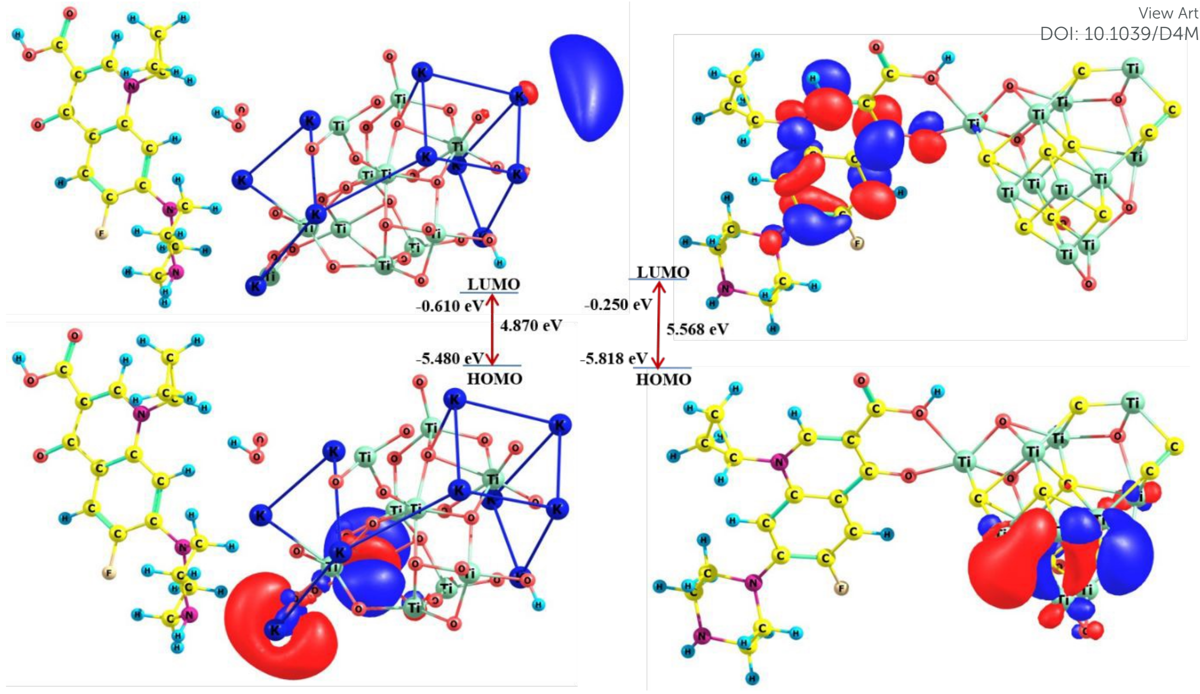

Figure 2. The three-dimensional (3D) HOMO-LUMO Isosurface Maps of the Dimer Complexes (left: KTNR-ciprofloxacin and right: MXene-ciprofloxacin) (bottom: HOMO and top: LUMO).

Finally, the FMOs such as HOMO, LUMO, and single-occupied molecular orbital (SOMO) have had a significant role in electronic transition phenomenon [43]. The HOMO of the KTNR-ciprofloxacin complex was distributed over only some of the Ti-metals of the KTNR component whereas importantly, a SOMO appeared to be located near a single K-metal atom. Very interestingly, the HOMO of the MXene-ciprofloxacin was spread over the some of the Ti-C bonds while the LUMOs were revealed to distributed over the C-atoms of two benzene rings which demonstrated to show π to π* transition.

3.2. XRD Analysis

The XRD pattern in the image is consistent with the conversion of Ti_3AlC_2 MAX Phase to $Ti_3C_2T_x$ MXene followed by conversion to KTNR (**Fig. 3(A)**). The presence of a high-intensity peak of the precursor Ti_3AlC_2 MAX phase at an angle of $2\theta = 38.9°$ at (104) signifies elemental Al. After being etched with HF, the layers become more separated and the peak (104) disappears which denotes the removal of Al. The diffraction peaks at (002), and (004) were assigned for $Ti_3C_2T_x$ MXene. This increases the d-spacing of the (002) peak, which can be observed as a shift of the peak to a lower angle in the XRD pattern [44]. The successful synthesis of delaminated Mxene was followed by hydrothermal synthesis of KTNR.

To comprehend the structure in details, $K_2Ti_4O_9$ crystallizes in the monoclinic C2/m space group [45]. There are two inequivalent K^{1+} sites. In the first K^{1+} site, K^{1+} is bonded in a 8-coordinate geometry to eight O^{2-} atoms. There are a spread of K-O bond distances ranging from 2.78-3.01 Å. In the second K^{1+} site, K^{1+} is bonded in a 6-coordinate geometry to six O^{2-} atoms. There are a spread of K-O bond distances ranging from 2.68-3.08 Å. There are four inequivalent Ti^{4+} sites. In the first Ti^{4+} site, Ti^{4+} is bonded in a 6-coordinate geometry to six O^{2-} atoms. There are a spread of Ti-O bond distances ranging from 1.76-2.27 Å. In the second Ti^{4+} site, Ti^{4+} is bonded to six O^{2-} atoms to form a mixture of distorted corner and edge-sharing TiO_6 octahedra. The corner-sharing octahedral tilt angles are 32°. There are a spread of Ti-O bond distances ranging from 1.77-2.22 Å. In the third Ti^{4+} site, Ti^{4+} is bonded in a 6-coordinate geometry to six O^{2-} atoms. There are a spread of Ti-O bond distances ranging from 1.73-2.35 Å. In the fourth Ti^{4+} site, Ti^{4+} is bonded to six O^{2-} atoms to form a mixture of distorted corner and edge-sharing TiO_6 octahedra. The corner-sharing octahedral tilt angles are 30°. There are a spread of Ti-O bond distances ranging from 1.79-2.19 Å. There are nine inequivalent O^{2-} sites. In the first O^{2-} site, O^{2-} is bonded in a distorted rectangular see-saw-like geometry to two equivalent K^{1+} and two Ti^{4+} atoms. In the second O^{2-} site, O^{2-} is bonded in a distorted single-bond geometry to six K^{1+} and one Ti^{4+} atom. In the third O^{2-} site, O^{2-} is bonded to two equivalent K^{1+} and two Ti^{4+} atoms to form distorted OK_2Ti_2 tetrahedra that share corners with two equivalents OK_2Ti_2 tetrahedra, corners with five OTi_4 trigonal pyramids, and an edge-edge with one OTi_4 trigonal pyramid. In the fourth O^{2-} site, O^{2-} is bonded in a distorted rectangular see-saw-like geometry to two equivalent K^{1+} and two Ti^{4+} atoms. In the fifth O^{2-} site, O^{2-} is bonded in a distorted linear geometry to two equivalent K^{1+} and two Ti^{4+} atoms. In the sixth O^{2-} site, O^{2-} is bonded in a 4-coordinate geometry to four Ti^{4+} atoms. In the seventh O^{2-} site, O^{2-} is bonded to four Ti^{4+} atoms to form distorted OTi_4 trigonal pyramids that share corners with three equivalents OK_2Ti_2 tetrahedra, corners with three OTi_4 trigonal pyramids, and edges with two equivalent OTi_4 trigonal pyramids. In the eighth O^{2-} site, O^{2-} is bonded in a 3-coordinate geometry to three Ti^{4+} atoms. In the ninth O^{2-} site, O^{2-} is bonded to four Ti^{4+} atoms to form distorted OTi_4 trigonal pyramids that share corners with two equivalents OK_2Ti_2 tetrahedra, corners with three OTi_4 trigonal pyramids, an edge-edge with one OK_2Ti_2 tetrahedra, and edges with four OTi_4 trigonal pyramids.

The XRD also suggested a Monoclinic phase indexing having a Bravais lattice space group C2/m. The unit cell had parameters a=18.25 Å, b=3.791 Å, c=12.01 Å, β=106.4 Å, and volume

Å^3. The diffraction angles with corresponding h k l values and d-spacing was calculated as (2 0 2), 2θ= 20.696, d= 4.2882 nm; (1 1 0), 2θ= 23.997, d= 3.705 nm; (0 2 0), 2θ= 47.953, d= 1.8955 nm. There are also some unidentified peaks present in the XRD pattern, which could be due to impurities or minor phases in the sample. It was evident that MXene had been successfully converted to KTNR after undergoing oxidation and alkalization [26] considering that the measured peak positions and intensities are consistent with those of JCPDS No: 32-0861 for $K_2Ti_4O_9$ (KTNR).

3.3. FESEM, EDAX, and Mapping analysis

The surface morphology of the materials was confirmed using FESEM performed for $Ti_3C_2T_x$ MXene which clearly showed stacking between the multi-layered structure (**Fig. 3(B)**) [46]. The width of ultrafine layers corresponded to a range varying from 6.76 nm to 12.62 nm. The inter-spacing between the layers ranged from 20 nm to 550. The FESEM images of KTNR depicted a distinct webbed-like complex network of nanoribbons having high surface area and porosity (**Fig. 3(C)**). The width/diameter of nanoribbons ranged from 9.7 nm to 16.4 nm indicating the uniformed morphology. Further, the EDAX and Mapping was done to obtain the atomic weight distribution (Wt%) K, Ti, and O relating to 41.5 %, 39.8 % and 15.3% respectively throughout the matrix correlating to successful synthesis of KTNR. The uniform abundance of all procured elements K, Ti, and O (**Fig. 3(D-E)**) which makes it a perfect candidate to achieve enhanced electrocatalytic activity of the nanocomposite especially due to notable presence of bimetallic Potassium and Titanium in the matrix. The presence of Carbon (3.4 Wt%) as recorded in EDAX was subjected probably due to some incomplete alkalization its precursor MXene.

3.4. HRTEM and SAED pattern analysis

HRTEM images further revealed the structural evolution from MXene nanosheets to KTNR nanoribbons. Aa simultaneous oxidation and alkalization process, the KTNR was assumed to have a diameter of around 10 nm (**Fig. 3(F-H)**). As shown in Fig. , HRTEM images validated the ultrafine widths as low as that of ~ 2.3 nm and ultrathin thickness of ~ 1.6 nm while the lattice spacings averaged at 0.745 nm. The width or thickness is comparatively lesser than that of precursor Ti_3C_2 MXene and thereby demonstrating the advantages of the morphological advancement in the nano-scale. Also, the HR-TEM results suggests that the KTNR exists in single or few layers which is practically impossible to achieve in MXene. In a polycrystalline material having monoclinic phase, the electrons will diffract at a range of angles, producing

View Article Online
DOI: 10.1039/D4MA01245C

rings on the SAED pattern. KTNR also showed multiring SAED pattern that confirmed the polycrystalline nanostructures with distinct phases (**Fig. 2(I)**).

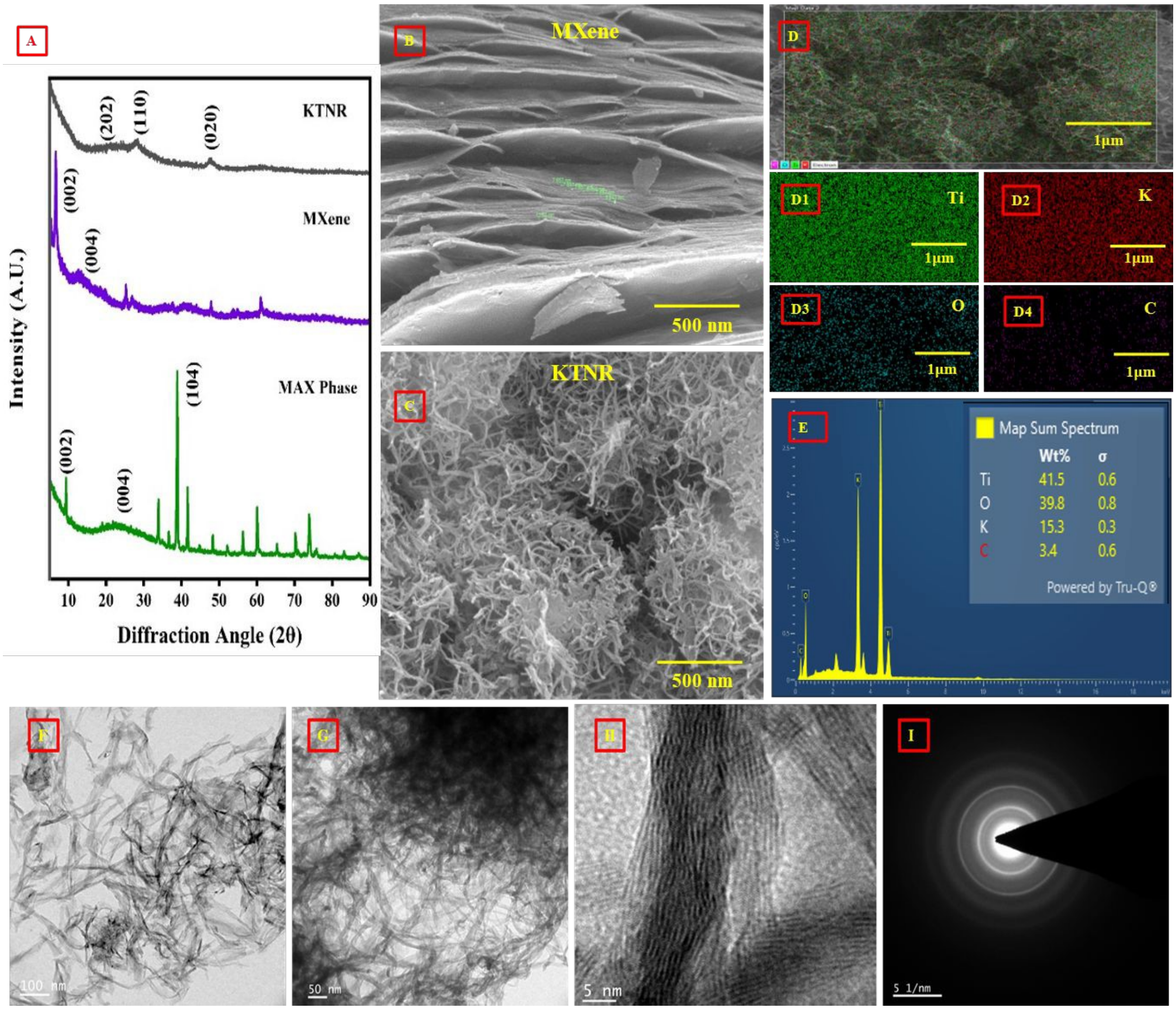

Figure 3. (A) XRD analysis of KTNR, Mxene and, MAX Phase in the range of (2θ) 5-90°; FE-SEM images of (B) MXene, (C) KTNR; Elemental mapping of (D) all elemental compositions together in KTNR; Atomic distribution of (D1) Titanium, (D2) Potassium, (D3) Oxygen, and (D4) Carbon in a selected section of the matrix of KTNR; (E) EDAX spectrum of elements of K:Ti:O:C; HR-TEM of KTNR at (F) 100 nm, (G) 50 nm and, (H) 5 nm scales showing different lattices including multiring SAED pattern (I) to confirm its polycrystallinity.

3.5. Surface optical profilometry, AFM, and Contact angles

View Article Online
DOI: 10.1039/D4MA01245C

The **Fig. 4(A1 and A2)** showed a line profile obtained from surface profilometry, likely representing the height variations along a specific line on the GCE surface. The provided data likely corresponded to specific roughness parameters measured by the profilometer. The roughness of the surface can influence the performance of the electrode in electrochemical applications. A moderately rough surface can provide more active sites for reactions compared to a flat surface. The both MXene (41319.6231 nm) and KTNR (41249.6805 nm) showed similar R values, indicating comparable overall roughness across the measured profiles. MXene (44811.3649 nm) has a higher M value compared to KTNR (43641.228 um). A higher M value signifies more prominent height variations throughout the profile. Both materials likely introduce roughness, potentially increasing the surface area for improved sensor performance. MXene might have had a surface with sharper peaks and valleys compared to KTNR, based on the higher M value. The width values (around 0.89 um for both) might represent the width measured at a specific height threshold and may not reflect the actual width of the MXene sheets or the average width of the KTNR nanoribbons. The position values (around 1.56 um for both) corresponded to the location where the ASH (average surface height) was measured. MXene (3491.74 nm) has a higher ASH compared to KTNR (2391.91 nm). This suggested that the MXene layer sits higher on average relative to the reference plane compared to the potassium titanate nanoribbons. Increased surface roughness and higher ASH could be beneficial for electrochemical sensors by providing more sites for analyte molecules to adsorb. This could potentially improve the sensitivity of the sensor. However, the optimal surface characteristics depend on the specific target analyte and the desired electrochemical process. Both MXene and KTNR appeared to introduce roughness to the GCE surface, which could be advantageous for sensor applications. MXene might offer a slightly higher surface area due to its roughness characteristics and higher average surface height. However, further analysis and testing are necessary to determine how these surface properties translate to sensor performance for specific target molecules. However, excessively rough surfaces can hinder electron transfer kinetics.

To consider AFM, both MXene and KTNR had an image size of 2 µm, indicating the area scanned by the AFM tip (**Fig. 4(B1-B2)**). This allowed for a direct comparison of the surface features within this defined area. The area (4.031 pm²) was identical for both samples as it represents the total analysed surface area by the AFM, which was likely the same for both measurements. The surface topography parameters i.e., Sa (Surface Area) for MXene (73.43 nm) had a significantly higher Sa compared to potassium titanate nanoribbons (30.255 nm).

View Article Online
DOI: 10.1039/D4MA01245C

This suggested a much larger projected surface area for MXene within the scanned area. This might be due to the inherent roughness of multi-layered MXene sheets compared to the smoother surface of individual few-layered KTNR nanoribbons. MXene (108.56 nm) also had a higher Sq (Root Mean Square Roughness) value compared to KTNR (42.233 nm). This confirmed that the MXene surface exhibited more significant height variations, indicating a rougher topography. A much higher Sy (Skewness) value for MXene (1057.6 nm) was compared to KTNR (332.57 nm). Both values were positive, suggesting surfaces with more frequent peaks than valleys. However, the significantly higher value for MXene indicated a much stronger tendency towards a peak-dominated surface profile. MXene (436.12 nm) also had a higher Sp (Peak Area Fraction) value compared to potassium titanate nanoribbons (181.4 nm). This aligned with the other parameters and suggested that the MXene surface has a larger portion covered by peaks compared to valleys. Both Sv (Valley Area Fraction) values were negative, which might be an artifact as discussed previously. However, the absolute value of Sv was much higher for potassium titanate nanoribbons (-151.17 nm) compared to MXene (-621.52 nm). It might also suggest a slightly higher portion of the scanned area for potassium titanate nanoribbons was covered by valleys compared to MXene. Sm (Mean Height) values were negative, indicating the surfaces were lower than the reference plane on average. However, the MXene surface has a slightly more negative Sm value (-10.028 pm) compared to potassium titanate nanoribbons (-10.015 pm). The AFM data suggested a clear difference in surface topography between MXene and potassium titanate nanoribbons. MXene exhibited a significantly rougher surface with larger height variations, a stronger tendency for peaks, and a larger portion of the surface covered by peaks. In contrast, the potassium titanate nanoribbons appeared to have a smoother surface with less pronounced height variations and a more balanced distribution of peaks and valleys (considering the uncertainty with Sv). The rougher surface of MXene, characterized by its higher Sa, Sq, Sy, and Sp values, could potentially offer a higher surface area for improved performance in electrochemical sensor applications. This increased surface area can provide more active sites for analyte molecules to adsorb, leading to potentially higher sensitivity. However, considering thin film formation, the higher surface roughness of the MXene film suggested a potentially larger effective surface area for applications like catalysis or electrochemical sensing. However, it might also hinder electron transport in electronic devices. The flatter and smoother potassium titanate nanoribbon film might offer less surface area but could potentially allow for more efficient electron transfer

View Article Online
DOI: 10.1039/D4MA01245C

across the electrode surface. Further analysis and testing are necessary to determine how these surface properties translate to sensor performance for specific applications.

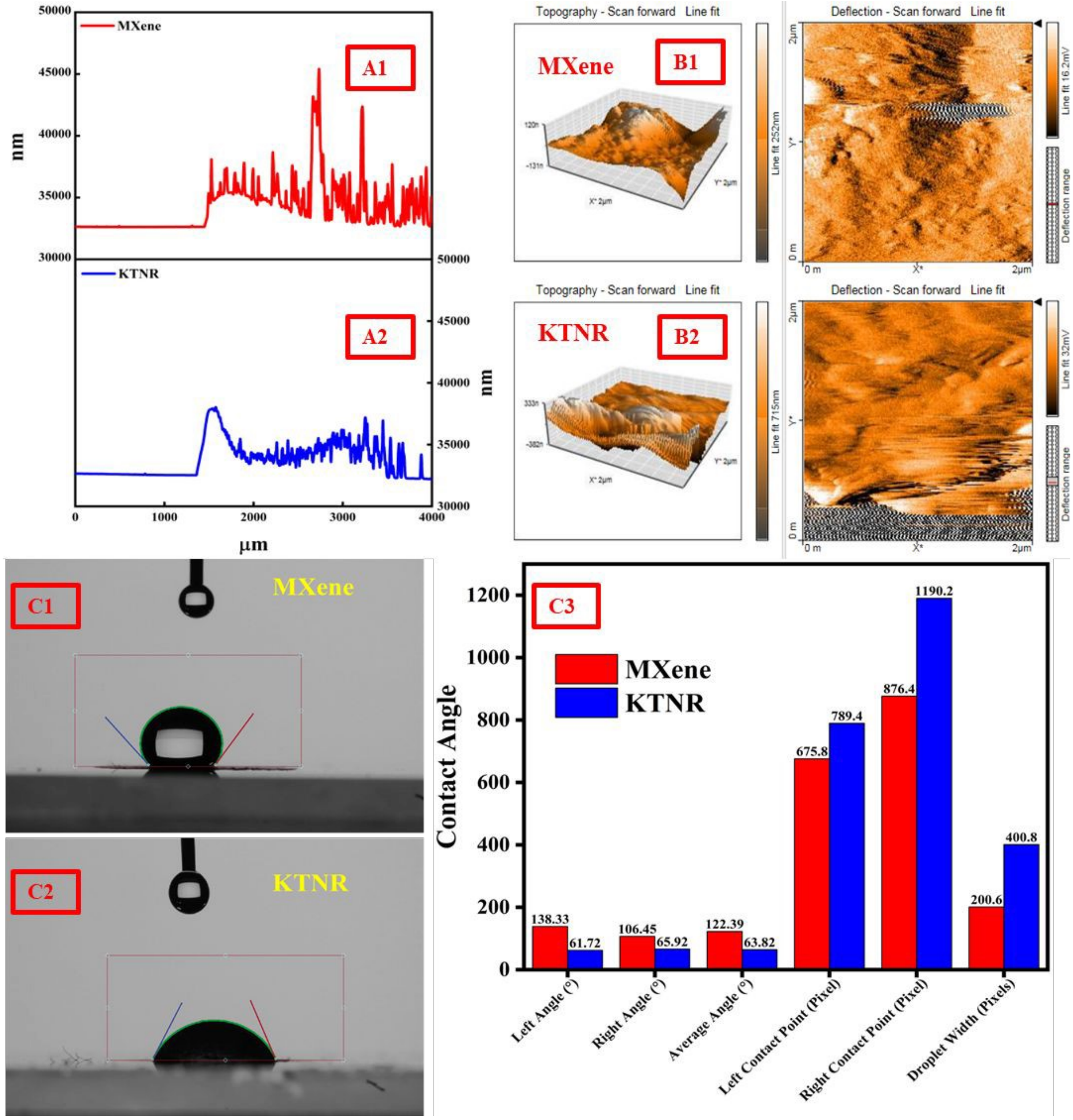

Figure 4. Surface optical profilometry of (A1) MXene and(A2) KTNR; AFM (3D) plot to show roughness characteristics and topography for (B1) MXene (B2) KTNR; Contact angle of 0.1 M phosphate buffer on the surface of (C1) MXene and (C2) KTNR fabricated GCE; (C3) Bar graph comparing parameters for Contact angle analysis.

The provided **Fig. 4(C1 and C2)** presented the contact angles measured between a drop of 0.1 M Phosphate buffer electrolyte and the surface of the MXene and KTNR fabricated GCE. The average contact angle for MXene (122.39°) indicated a hydrophobic surface whereas the average contact angle of KTNR (63.82°) suggested a hydrophilic surface. Generally, a moderately hydrophilic surface was preferred for electrochemical sensors. This allows for good wettability by the electrolyte solution while maintaining some degree of control over the adsorption/desorption processes of analyte molecules at the electrode surface. A low contact angle like that of KTNR indicates good wettability, meaning the electrolyte can easily penetrate the electrode pores and reach the active material. This is essential for efficient ion transport and redox reactions. Proper wetting ensures good contact between the electrolyte and the electrode surface, facilitating fast charge transfer and improving the overall kinetics of the electrochemical process. Highly hydrophobic surfaces can hinder electrolyte interaction and limit sensor performance. Highly hydrophilic surfaces might allow for excessive non-specific adsorption of molecules from the electrolyte, leading to background noise and decreased sensor sensitivity [47]. Based on the contact angle data, KTNR with a more hydrophilic surface (average angle of 63.82°) appeared to be a better candidate for an electrochemical sensor compared to MXene (average angle of 122.39°). A bar graph is provided to represent the parameters owing to calculation of contact angle (**Fig. 4(C3)**). The surface roughness could influence the effective contact angle. Rougher surfaces could exhibit higher contact angles even for hydrophilic materials like MXene in this case. The specific target analyte and the desired electrochemical process could also play a role in determining the optimal surface wettability. Other factors like surface chemistry and charge distribution could also influence the interaction between the electrode surface and the analyte/electrolyte. While the contact angle data suggested KTNR might be more favourable due to their hydrophilicity, further testing with the target analyte and optimization of the electrode surface properties would be necessary to achieve the best performance for a specific electrochemical sensing application.

3.6. Material characterizations and electrochemical techniques

3.6.1. Stability study for MAX Phase, MXene, and KTNR fabricated GCE

The experiment was performed to compare the stability of MAX Phase, MXene and KTNR and electrodes for 5 mM $K_3[Fe(CN)_6]$ oxidation in 0.1 M KCl solution over multiple CV cycles (10 and 100 cycles) ((**Fig.5A(1-2), Fig.5B(1-2)** and **Fig.5C(1-2)**) [48]. The current values and their standard deviations were provided for each electrode at different cycle numbers. All electrodes fabricated with MAX Phase, MXene, and KTNR showed a decreasing trend in current with increasing cycle number. For MAX phase, MXene, and KTNR, the current value starts at 1.27 µA, 5.44 µA, and 5.51 µA in 10 cycles and decreases to 1.15 µA, 4.24 µA and 4.37 µA at 100 cycles. This suggests a loss of electrocatalytic activity for KTNR over time. The MAX Phase and MXene fabricated electrodes showed a huge drip in current with consecutive cycles, but the change of current at the oxidation peak is less pronounced while compared to KTNR, which showed a broad error bar. The standard deviations for both electrodes are relatively small compared to the current values, indicating good reproducibility of the measurements. The alternate increase and decrease in current density suggested a loss of electrocatalytic activity over time, could be due to several factors. The MAX Phase, MXene or KTNR nanostructures could be degrading during the cycling process which could be due to the electrochemical breakdown of the materials or the dissolution of metal ions from the electrode [49]. The surface of the electrodes could be fouled by reaction products or other impurities in the electrolyte [50]. This would block the active sites on the electrode and hinder electron transfer. Lastly, the electrode-electrolyte interface could be weakening over time. This would lead to an increase in resistance and a decrease in current density. The stability of KTNR can be compared to MXene and MAX Phase by comparing the decrease in current density for both materials over the same number of cycles. A smaller decrease in current density for KTNR indicated better stability. However, if the anodic peak currents of KTNR and MXene are to be compared, KTNR shows much significant current 4-5 folds greater than that of MXene and MAX Phase fabricated electrodes over multiple cycles (**Fig. 5(D)**). The cathodic current represents the reduction process. The cathodic current was observed to be higher for KTNR in both the 10-cycle and 100-cycle tests. The potential range for all three materials was similar, suggesting that the differences in current are not due to a wider electrochemical window for KTNR. The possibilities, owing to large cathodic current, might be related to KTNR, being nanoribbons, likely possessed a higher surface area compared to MXene and MAX Phase fabricated GCE. A larger surface area is ought to provide more active sites for electrochemical reactions, leading to increased current. The potassium ions in KTNR may interact with the redox species ($Fe(CN)_6^{3-}$) in the electrolyte, leading to a synergistic effect that enhances the reduction process. The unique structure of KTNR might have facilitated faster charge transfer during the reduction process which could be due to efficient ion diffusion within the nanoribbons or other factors related to their crystal structure. Hence, KTNR exhibited better electrochemical stability, especially over multiple cycles. That would mean that the material could maintain the active sites and charge transfer capabilities, resulting in sustained high cathodic current even after repeated cycling [51,52]. Also the broad window of MAX Phase and MXene suggeted them

View Article Online
DOI: 10.1039/D4MA01245C

to be energy staorage materials while KTNR exhibits a way better catalytic property as an electrode material.

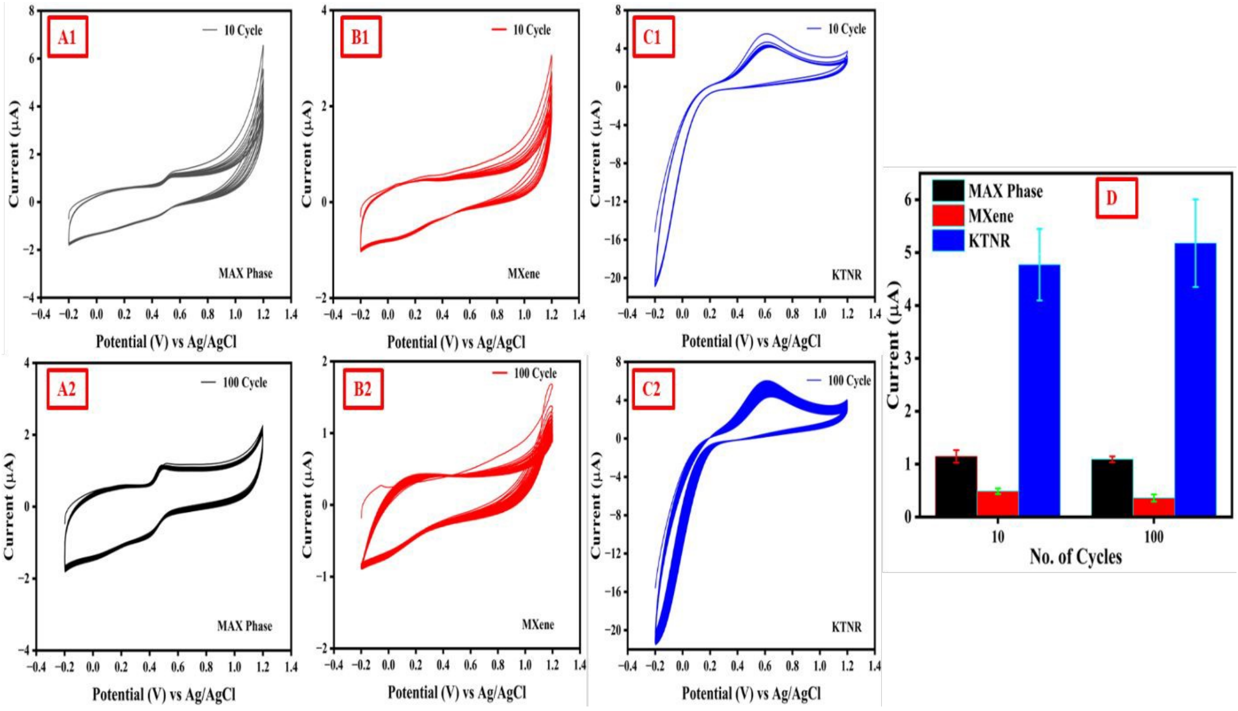

Figure 5. Stability Study of (A1-A2) MAX Phase/GCE, (B1-B2) MXene/GCE and KTNR (C1-C2) employing 10-200 cycles in 5 mM $K_3[Fe(CN)_6]$; (D) Error Bar graph showing peak currents against 10 and 100 cycles for MAX Phase, MXene and KTNR.

3.6.2. Understanding the properties of electrode materials using various electrochemical techniques

The intricate properties of all electrode materials were subjected to electrochemical techniques such as CV, DPV, and EIS in 5mM $K_3[Fe(CN)_6]$ containing 0.1 M KCl. The electrocatalytic properties of KTNR, MXene, and MAX Phase were studied through CV and DPV. The CV and DPV voltammograms suggest that KTNR-fabricated GCE exhibited highest electron transfer compared to MXene and MAX Phase fabricated GCEs. The CV graph (**Fig. 6(A)**) was observed to have a sharp peak of KTNR having an I_{pa} almost 4 times anodic peak current (I_{pa} = 3.96 µA) which demonstrated faster reaction kinetics while MXene and MAX Phase having I_{pa} = 0.69 µA and 0.38 µA respectively, had much broader peaks, indicating a slower reaction. It was also confirmed by DPV (**Fig. 6(B)**) where a high peak current in the KTNR (I_{pa} = 1.15 µA) curve was observed compared to MXene (I_{pa} = 0.98 µA) and MAX Phase (I_{pa} = 0.46 µA) indicated greater electrode activity for the redox reaction of $K_3[Fe(CN)_6]$. A more positive peak potential for KTNR (E_{pv} = 0.39 V) signified a lower overpotential, meaning the electrode requires less or optimal energy to drive the reduction reaction compared to MXene (E_{pv} = 0.43 V) and MAX Phase (E_{pv} = 0.16) [53]. The effective surface area by KTNR, MXene and MAX Phase fabricated electrodes were calculated to be 3.47×10^{-8} cm^2/s, 1.054×10^{-9} cm^2/s and 3.196×10^{-10} cm^2/s respectively. By considering all parameters, MXene and MAX Phase as electrode materials were ought to be better as energy storage materials while KTNR showed better electro-catalytic performance.

The EIS Nyquist plots for KTNR fabricated GCE shows a lower impedance compared to its precursors MXene and MAX Phase. This indicates that the KTNR electrode has a higher ability to transfer charge at the electrode-electrolyte interface. In other words, it has better electrocatalytic activity [54]. . In the Nyquist plot, the imaginary impedance (Z") is plotted on the y-axis and the real impedance (Z') is plotted on the x-axis (**Fig. 6(C)**). The equivalent circuit model simplified KTNR electrode-electrolyte interface and the fitting method used was Randomize + Simplex while the parameters were the values of the components in the equivalent circuit (R_1+Q_1/(R_2+C_2/(R_3+C_3/(R_4+W_4)))+C_5/R_5) that best match the experimental EIS data. The R_1 = 2.028 Ω or the solution resistance (R_s) represented the resistance of the electrolyte solution between the working and reference electrodes. A lower R_s suggests a more conductive electrolyte solution. The R_2 =195 Ω and R_3 = 938.9 Ω referred to charge transfer resistance (R_{ct}) that represented the resistance to electron transfer between the electrode and the electrolyte. The Nyquist plot showed a smaller semicircle diameter at low frequencies indicates a lower R_{ct} and faster charge transfer kinetics [55]. In the image, the KTNR electrode has a smaller semicircle diameter compared to MXene and MAX Phase. The diameter of the semicircle for KTNR extends less towards the lower frequencies, it could also indicate faster mass transfer for the KTNR electrode. The value of R_4 = 23601 Ω suggested a Warburg impedance W_4 = 0.2033e-9 Ohm.$s^{-1/2}$ implying to the resistance to mass transfer of ions within the electrolyte which in-turn was related to the rate of the reaction at the electrode surface [56]. The possible film resistance R_5 = 271304 Ω represented the resistance of Nafion stabilized KTNR thin film formed on the electrode surface. The C_2 = 0.509e-6 F or the double layer capacitance represented the capacitance between the electrode-electrolyte interface. The C_3 = 0.2197 µF and C_5 = 1.287e24 F represented capacitance associated with the Nafion stabilized film on the electrode surface or porosity of KTNR as electrode material [57]. Lastly, Constant Phase Element (Q_1 = 4.239e-6 F.s^{a-1}) was an element that could be used to model a more complex capacitance where the parameter "a1= 0.7535" determined the deviation from ideal capacitance behaviour of the equivalent circuit. The exchange current density represents the rate of electron transfer at equilibrium, where the forward and reverse reaction rates are equal.

It's a fundamental parameter that reflects the intrinsic activity of the electrode material. The key relationship is derived from the Butler-Volmer equation, and under conditions of small overpotential (near equilibrium), it simplifies to $I_0 = RT / (nF\ Rct)$; where I_0 = exchange current density (A/cm²), R = ideal gas constant (8.314 J/mol·K), T = absolute temperature (K), n = number of electrons transferred in the redox reaction, F = Faraday constant (96485 C/mol) and Rct = charge-transfer resistance (Ω). The Rct values in this case was calculated to be 938.9 Ω, 230346 Ω and 326328 Ω for KTNR, MXene and MAX Phase respectively which yielded the corresponding I_0 values of 2.75×10^{-5} A/cm², 1.22×10^{-7} A/cm² and 7.92×10^{-8} A/cm². The exchange current density showed KTNR/GCE has much better intrinsic electrocatalytic activity[58].

A Bode plot ((**Fig. 6(D1-D2)**) typically shows two key features for EIS data, one being the phase angle which indicates the phase shift between the applied voltage and the resulting current and second is impedance magnitude (log |Z|) which represents the overall resistance to current flow in the system. At high frequencies, the phase angle typically approached towards 0 degrees, indicating minimal phase shift. As the frequency decreases, the phase angle becomes more negative, reflecting the increasing influence of capacitive behaviour. At even lower frequencies, the phase angle might approach -90 degrees for a purely capacitive response. At high frequencies, the impedance magnitude was usually dominated by solution resistance and shows a plateau in the log |Z| vs. log |f| plot. As the frequency decreases, the impedance magnitude might start to increase due to the influence of charge transfer resistance and other processes. The provided information suggested a complex equivalent circuit model was used to capture the EIS response of the KTNR, MXene, and MAX Phase fabricated GCE.

View Article Online
DOI: 10.1039/D4MA01245C

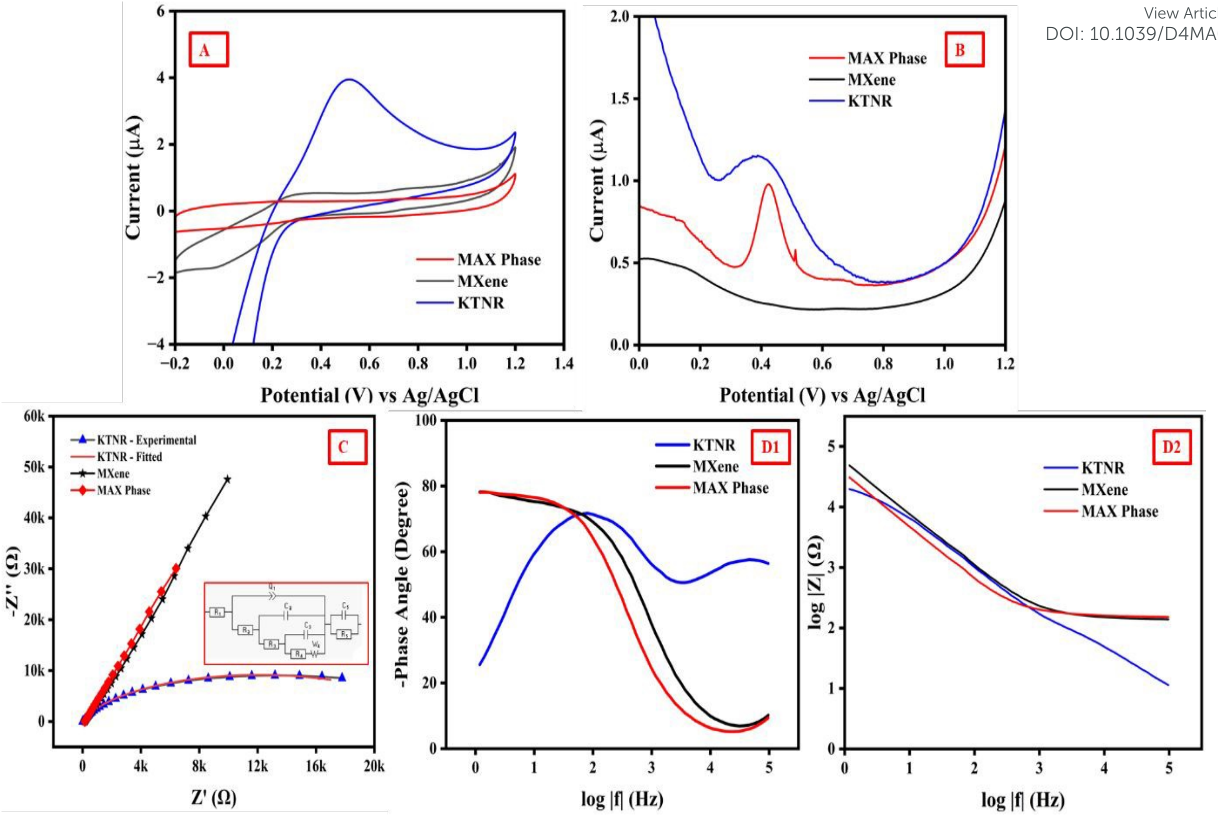

Figure 6.(A) CV (B) DPV (C)EIS Nyquist plots (inset: Equivalent Circuit) (D) Bode Plot for KTNR, MXene and MAX Phase fabricated GCE in 5 mM $K_3[Fe(CN)_6]$ in 0.1M KCl electrolyte.

3.6.3. Mechanism of electro-oxidation of ciprofloxacin on active working surface area of KTNR fabricated electrode

Ciprofloxacin is a fluoroquinolone antibiotic known for its broad-spectrum activity. It is a zwitterionic molecule, meaning it can exist with both positive and negative charges depending on the pH. KTNR is a metal oxide material having surface charge which can influence the interaction with ciprofloxacin molecules. The process of electrochemical oxidation involved the transfer of electrons from ciprofloxacin molecules to the electrode surface, resulting in the oxidation of ciprofloxacin. The steps involved were diffusion, adsorption, electron transfer, desorption and diffusion which can be observed in **Fig. 7(C)**. Ciprofloxacin molecules in the bulk solution diffuse towards the surface of the Potassium Titanate electrode. Ciprofloxacin molecules could interact with the electrode surface through various forces like electrostatic interactions, hydrogen bonding, or van der Waals forces. The net charge of ciprofloxacin at pH 8 (likely negatively charged) and the surface charge of the KTNR (which could also be pHdependent) would influence this adsorption process. At the electrode surface, ciprofloxacin molecules lose electrons to the electrode, undergoing oxidation. The specific mechanism of electron transfer could involve direct interaction with the electrode or the participation of intermediate species formed on the electrode surface. The oxidized ciprofloxacin molecules desorbed from the electrode surface and get diffused back into the bulk solution. The factors that could affect the process are pH, electrode potential and scan rate. The pH of the solution could influence the net charge of ciprofloxacin and the surface charge of the KTNR electrode. An optimal pH might exist for balancing the electrostatic interactions and promoting efficient electron transfer. The applied potential at the electrode can influence the rate of electron transfer. A higher positive potential might be required to drive the oxidation reaction. In cyclic voltammetry experiments, the scan rate can affect the observed current response. At faster scan rates, the diffusion process might become limiting, leading to a deviation from the ideal behaviour. The electrochemical oxidation of ciprofloxacin at a Potassium Titanate electrode ought to be a complex process involving mass transport (diffusion), surface interaction (adsorption/desorption), and electron transfer. The efficiency of this process depended on various factors like pH, electrode potential, and surface properties which were studied and optimized in the later part of the research.

3.6.4. Optimization of pH for ciprofloxacin detection using KTNR/GCE

Ciprofloxacin is a zwitterionic molecule, meaning it can exist with both positive and negative charges depending on the pH. At lower pH (around 4), ciprofloxacin is likely mostly protonated (positively charged) due to the acidic environment. As observed in **Fig. 7(A1-A2)** the pH increases from 4 to 11, the solution becomes more basic, and ciprofloxacin loses its protons, becoming increasingly deprotonated (negatively charged). To deal with surface charge interaction KTNR being a metal oxide material that also exhibited a surface charge depending on the pH. At lower pH, the KTNR active surface might be positively charged. As the pH increased, the surface charge of KTNR could become more negative. When the pH was low (acidic), both ciprofloxacin (positively charged) and the KTNR surface (positively charged) experienced electrostatic repulsion. This repulsion could hinder the adsorption of ciprofloxacin molecules onto the electrode surface and slow down the electron transfer process. As the pH increased, ciprofloxacin became increasingly deprotonated (negatively charged). This could lead to attractive forces between the negatively charged ciprofloxacin and the potentially negatively charged KTNR surface at higher pH. This attraction could enhance the adsorption of ciprofloxacin molecules and potentially promote the electron transfer process, leading to a higher current at a slightly less positive potential (anodic shift). The observed optimal pH of 8 might be a balance between these two effects. At pH 8, ciprofloxacin might be sufficiently deprotonated to favour adsorption on the electrode surface while minimizing any repulsion from the electrode surface itself. Since the pH 8 is between the reference pKa values (pKa1 = 5.17 and pKa2 = 8.74), ciprofloxacin will likely exist in a zwitterionic form in the 0.1 M pH 8 phosphate buffer. The carboxylic acid group (pKa1) will likely be deprotonated (negatively charged) as the solution's pH is higher than its pKa. The primary amine group (pKa2) might be partially protonated (positively charged) due to the pH being slightly lower than its pKa2. This could lead to the most efficient electron transfer and the highest anodic peak current for ciprofloxacin oxidation. The anodic peak shifted towards more positive potentials with increasing pH suggesting a change in the rate of the electro-oxidation reaction. The shift likely reflected a slower reaction rate at lower pH (due to electrostatic repulsion) and a potentially faster rate at higher pH (due to enhanced adsorption). Ciprofloxacin might undergo multiple redox reactions involving different electron transfers and protonations. This complex mechanism could lead to non-linear behavior, as the relative contributions of these reactions can vary with pH. Ciprofloxacin, like many drugs, exists in different protonation states depending on the pH of the solution [59]. These different protonation states could also have varying redox potentials, which might have led to non-linearity [60]. The nature of the electrode surface, including its composition and roughness, can influence the adsorption of ciprofloxacin and its redox behavior since the fabrication of electrode using drop-casting method might always lead to handling errors [61–63]. The ionic strength of the solution could also influence the activity coefficients of the species involved in the redox reaction, leading to deviations from the expected linear relationship [64–66]. Temperature could also be a parameter that might have influenced the kinetics of the redox reaction and the stability of the redox species [67,68]. This can further complicate the relationship between redox potential and pH .

3.6.5. Impact of scan rates on ciprofloxacin detection using KTNR/GCE

The CV curves showed anodic peaks around 0.8 V to 1.0 V at pH 8, which corresponded to the oxidation of ciprofloxacin. As the scan rate increased (from 1 mV/s to 200 mV/s), the following trends were observed (**Fig. 7(B1 and B3)**). The anodic peak current increased and the peak potential (where the current is maximum) shifted slightly towards more positive potentials. The linear regression plots of anodic current (I_p) vs. square root of scan rates ($v^{1/2}$) for three scan rate ranges (1-10 mV/s, 10-100 mV/s, and 100-200 mV/s) suggested a diffusion-controlled electrochemical process for ciprofloxacin oxidation at least for the lower scan rates (1-10 mV/s). The high R-squared values 0.97012 and 0.94887 for the linear plots I_p = 9.99826E-7* $v^{1/2}$ + 2.69476E-7 (**Fig. 7(B2)**) and I_p =7.4844 - 7* $v^{1/2}$ + 1.50171E-7 (**Fig. 7(B4)**) respectively, which indicated good linear relationships between the I_p vs $v^{1/2}$ in these two lower scan rate ranges. The deviation from linearity observed at higher scan rates (above 10 mV/s) might be due to limitations in the diffusion process of ciprofloxacin molecules towards the electrode surface at faster scan rates. The regression suggested a diffusion-controlled process. The number of electrons transferred (n) was 1 for ciprofloxacin oxidation and the concentration (C) of analyte was 90 µM. The electrode surface area (A) was calculated to be 0.071 cm^2 for GCE. The Diffusion coefficient (D) was calculated using Randles-Sevcik equation, with the formula: $I_p = (2.69 \times 10^5) * n^{3/2} * C * A * D^{1/2} * v^{1/2}$. The calculated average diffusion coefficient of 2.21E-11 cm²/s was well consistent within a reasonable range for ciprofloxacin in phosphate buffer electrolyte. Diffusion-Controlled Reactions: At slower scan rates, diffusion processes can become limiting, leading to a more reversible behaviour. As the scan rate increases, the system may not have enough time for the diffusion of reactants and products, leading to a deviation from reversibility and a crossover of the anodic and cathodic peaks.

The crossing of the CV curves at higher potentials in the 10 mV/s to 200 mV/s scan rate range suggested a change in the electrochemical behaviour of the system (**Fig. 7(B3)**). If the charge transfer kinetics were slow, increasing the scan rate could lead to a shift in the peak potentials and a crossover of the curves. At higher scan rates (>50mV/s), the capacitive current associated with double-layer charging became more significant [69]. This could contribute to the observed crossover, as the capacitive current can mask the faradaic current associated with the redox processes. At higher potentials beyond 1V, the electrode surface might undergo oxidation or reduction processes that affected the electrochemical behaviour [70,71]. These changes could also lead to a shift in the peak potentials and a crossover of the curves [72,73]. PB electrolyte containing ciprofloxacin could have caused a potential drop (IR drop) across the electrolyte hemisphere, which might have distorted the CV curves, especially at higher scan rates. This IR drop could lead to a shift in the peak potentials and a crossover of the curves [74].

Based on the observed behaviour, a possible mechanism for ciprofloxacin oxidation at the KTNR/GCE could be proposed. Ciprofloxacin molecules in the bulk solution diffused towards the electrode surface. At the electrode surface, ciprofloxacin underwent an electron transfer reaction, getting oxidized. The oxidized ciprofloxacin got desorbed from the electrode surface and diffused back into the bulk solution. At slower scan rates, where the diffusion process was dominant, the current increased as the scan rate increases since there was more time for

View Article Online
DOI: 10.1039/D4MA01245C

ciprofloxacin molecules to diffuse towards the electrode surface and get oxidized. At faster scan rates, the diffusion process might become limited. The ciprofloxacin molecules might not be able to reach the electrode surface fast enough to keep up with the electron transfer reaction rate. This could lead to a deviation from the ideal linear relationship between the current and the square root of scan rate. The CV data suggested that the oxidation of ciprofloxacin at the KTNR/GCE was an electrochemically active process. The slight shift in the anodic peak potential with increasing scan rate might be due to kinetic limitations or a combination of diffusion and kinetic control at higher scan rates.

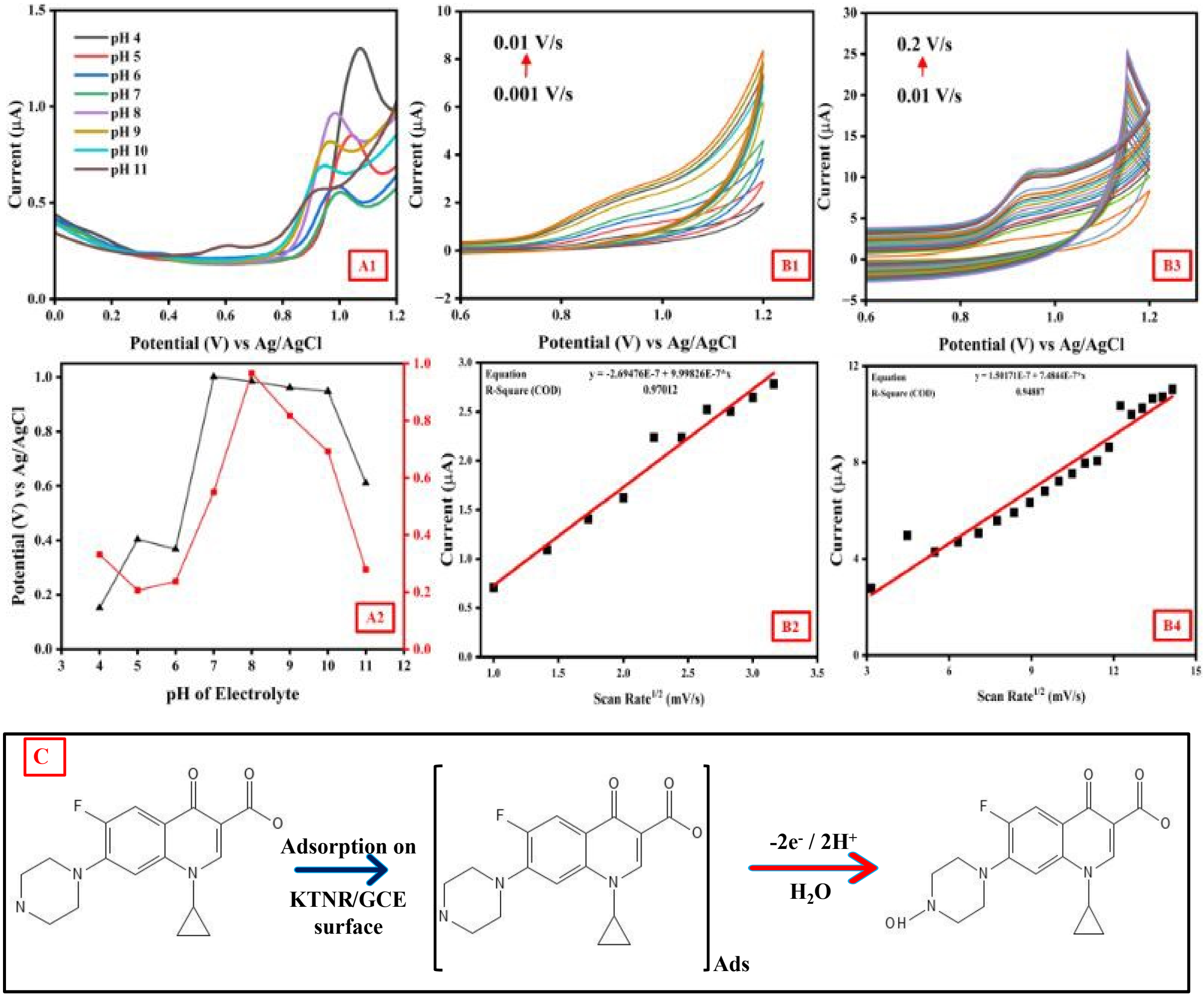

Figure 7. (A1) Study of pH to optimize the voltammetric detection of ciprofloxacin using KTNR/GCE, (A2) Line + Scatter plot to show the correlation of Peak potential (E_{pv}) and Anodic Peak Current (I_{pa}) vs pH of the 0.1M Phosphate Buffer electrolyte containing ciprofloxacin; Study of different scan rate CV (B1) 0.01-0.01 mV/s and (B3) 0.01-0.2 mV/s in 0.1M Phosphate Buffer at optimized pH =8 and, their corresponding regression plots

View Article Online
DOI: 10.1039/D4MA01245C

(B2 and B4); (C) Illustration of the mechanism of electro-oxidation of ciprofloxacin at the active surface area of KTNR/GCE.

3.6.6. Electrochemical sensing studies of ciprofloxacin using KTNR/GCE

The CV aimed to investigate the electrochemical response of ciprofloxacin at a KTNR/GCE in a linear concentration range of 0.6 µM to 147.2 µM (**Fig. 8(A1)**). The CV likely showed indistinguishable but linearly increasing oxidation peaks at a specific potential, indicating the electrochemical oxidation of ciprofloxacin at the KTNR/GCE. The position of this peak could be determined at beyond 1.0 V as observed in the voltagram. It was also observed that the oxidation peak current (I_{pa}) increased as the concentration of ciprofloxacin (C) in the electrolyte solution increased. Although no clear peaks were formed, the voltagram suggested that KTNR was actively involved in catalysis which indicated that more ciprofloxacin molecules were being oxidized at the electrode with higher concentrations. Ideally, the plot of peak current vs. ciprofloxacin concentration exhibited a linear relationship having an equation I_{pa} = 1.86503E-8*C + 9.36571E-7 with an R^2 = 0.94776 (**Fig. 8(A2)**) within a specific concentration range of 0.6 µM to 147.2 µM. The LOD was calculated to be 0.07 µM and LOQ was 0.213 µM. The sensitivity of the KTNR/GCE for ciprofloxacin sensing through CV was 0.282 µA uM^{-1} cm^{-2}.

DPV was used, which is a more sensitive technique compared to CV for quantitative analysis. The potential range scanned was from 0.6 V to 1.2 V (**Fig. 8(B1)**). The DPV plot showed a well-defined peak at a specific potential, corresponding to the oxidation of ciprofloxacin at the KTNR electrode. The E_{pv} = 0.98 was the peak voltage that could be determined from the voltagram. The image showed that the peak current for the ciprofloxacin oxidation peak increases with the concentration of ciprofloxacin in the electrolyte solution. One could analyze the linearity by plotting the peak current data points for different concentrations and fitting a straight line through them I_{pa} = 1.53611E-8*C + 2.32189E-7 and I_{pa} = 5.38365E-9*C + 5.36113E-7 (**Fig. 8(B2)**). The respective R^2 value of the fit i.e., 0.99273 and 0.9554, indicated how excellent the data corresponded to a linear relationship. Through DPV, the KTNR/GCE offered a sensitivity of 0.0986 µA uM^{-1} cm^{-2} , while having an LOD and LOQ of 0.0608 µM and 0.184 µM respectively.

View Article Online
DOI: 10.1039/D4MA01245C

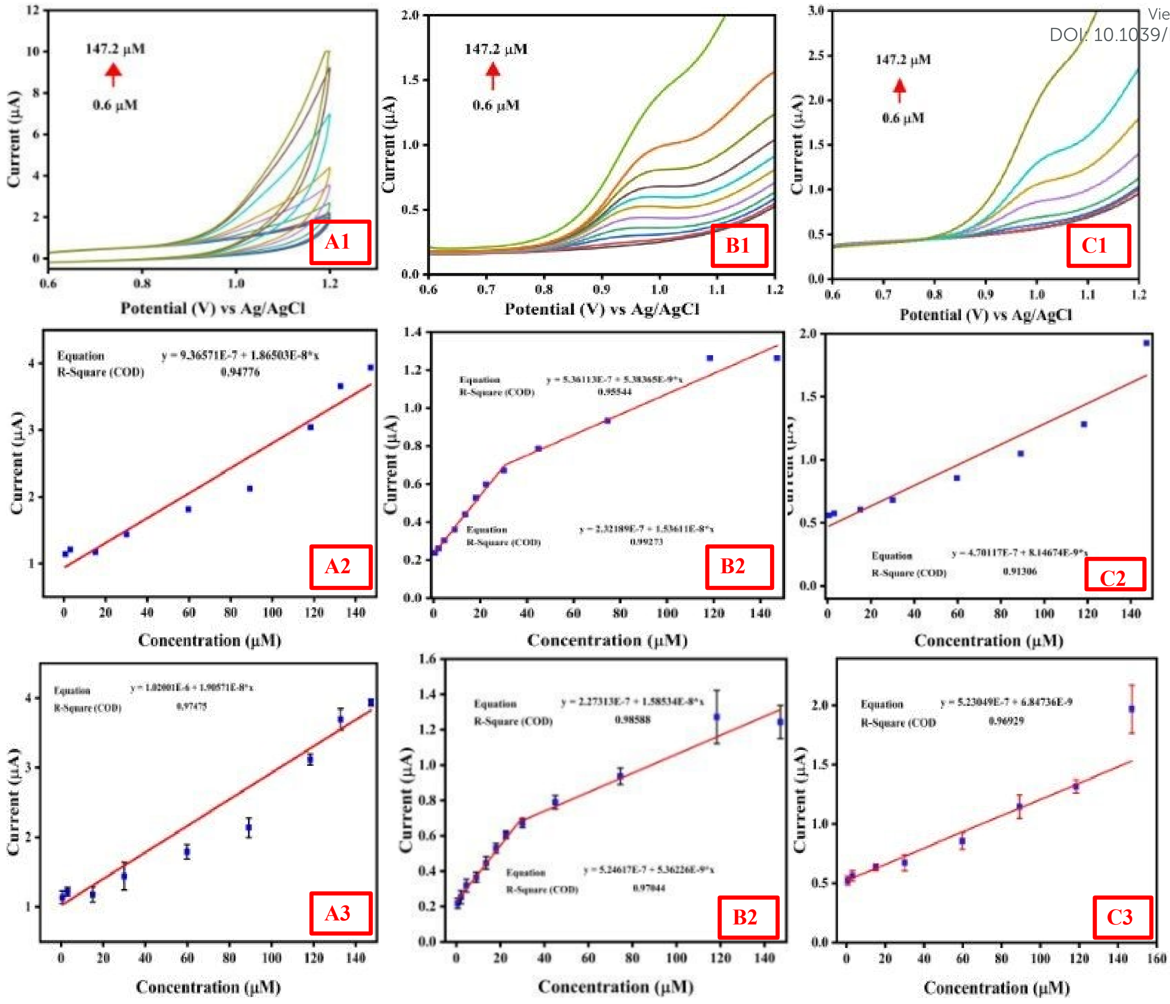

Figure 8.(A1 and A2) CV response and corresponding regression plot; (B1 and B2) DPV response and corresponding regression plot; (C1 and C2) SWV response and corresponding regression plot of KTNR to obtain the linear concentration range of ciprofloxacin in 0.1 M Phosphate buffer pH = 8; triplicate data on (A3) CV (B3) DPV and (C3) SWV response curves with regression plots showing excellent replicability.

SWV being a variant of pulse voltammetry, was employed to confirm linearity observed in DPV. It also offers advantages like higher sensitivity and lower background current compared CV. Each curve in the plot likely corresponded to the SWV response for a different concentration of ciprofloxacin in the electrolyte solution which also relayed to the oxidation at the KTNR active electrode surface (**Fig. 8(C1)**). The equations I_{pa} = 8.14674E-9*C + 4.70117E-8 with an R^2 value = 0.91306, shows its consistency with DPV results (**Fig. 8(C2)**). Also, the LOD and LOQ were calculated which yielded to be 0.0264 μM and 0.08 μM respectively, while offering a sensitivity of 0.113 μA uM^{-1} cm^{-2}. The replicability showed consistent replicability in data of CV, DPV and DPV as shown in **Fig. 8(A3,B3,C3).**

Overall considering highest sensitivity value and lowest LOD. The DPV data suggested that the KTNR/GCE electrode was a more promising tool for the quantitative detection of ciprofloxacin within a certain concentration range of 0.6 µM to 147.2 µM over CV and SWV. DPV and SWV minimizes the contribution of the charging current by measuring the current at specific points after the potential step. This led to a sharper and more well-defined peak compared to CV. The current measured with DPV and SWV was constant throughout the experiment which reflected the faradaic current at specific points in the potential waveform. This resulted in a more prominent current response compared to the smooth regular curve observed in CV. The observed increase in oxidation peak current with increasing concentration indicated a linear relationship that could be exploited for analytical purposes. This dynamic range of micromolar concentration can be used for quantitative analysis of ciprofloxacin concentration in unknown samples using the KTNR/GCE electrode. A comparison with previous reported non-enzymatic electrochemical sensors for ciprofloxacin detection is tabulated in **Table 2**.

Table 2. Reported literature on non-enzymatic electrochemical sensors for detection of ciprofloxacin

Materials/Electrode	Method	Linear Range (µM)	LOD (µM)	Real Samples	References
Co-MOFs/PLA	DPV	0.5–150	0.017	Drug	75
GO/SPCE	DPV	1-8	0.3	Milk	76
TiO2/PVA/GCE	DPV	10–120	0.04	Rain water	77
f-MWCNTs/PANI/GCE	LSV	0.1-1,1-20	0.08	Pharmaceuticals	78
f-MWCNT-coated GCE	SWV	5-100	0.16	Hospital effluent, wastewater, natural water	79
BaCuSi4O10/GCE	DPV	0.05-150	0.0009	Pharmaceuticals	80
Pt-RGO/GCE	DPV	10-25	1.53	Tap water, river water	81
CRGO/GCE	SWV	6-60	0.5	Pharmaceuticals, milk	82
Ch-AuMIP/GCE	DPV	1-100	0.21	Tap water, milk, mineral water, pharmaceuticals	83
BiPO4/GO-MMIPs/PGE	SWSV	39-740	0.4	Blood serum, milk	84
Fe-g-C3N4/PGE	DPV	0.001-1	0.0054	Blood serum	85

ChCl/CPE	SWV	0.005 -200	0.00036	CIP eye drops, eggs, river water	86
KTNR/GCE	CV, DPV, SWV	0.6 – 147.2	0.07, 0.0608, 0.0264	honey, milk, eggs, marine water, Ganga water, organic fertilizer, soil, Simulated body fluid	This work

3.6.7. Reproducibility of KTNR/GCE for ultrasensitive detection of ciprofloxacin

Freshly fabricated ten KTNR fabricated electrodes were tested through CV, DPV and SWV (**Fig. 9(A1, B1, and C1)**) in the same laboratory conditions and room temperature (25˚C) to check the reproducibility of the electrodes towards ciprofloxacin detection using CV technique at a random concentration. The system's viability was confirmed by an error bar graph (**Fig. 9(A2, B2 and C2)**) that practically demonstrates the stability of the electrode. The peak currents averaged at 0.91 µA ± 0.15%, 0.484 µA ± 0.19% and 1.2 µA ± 0.12% were obtained from CV, DPV and SWV. The results showed excellent reproducibility owing to the novelty of newly developed KTNR based electrochemical sensor. The variation estimated as RSD values of 0.15%, 0.19% and 0.12% was calculated which could be owed to the handling error and manual fabrication of the electrodes. However, if the sensor fabrication samples were not stored properly after preparation, the electrode materials of the sensor could be prone to oxidation and resulted in the performance might degrade.

View Article Online
DOI: 10.1039/D4MA01245C

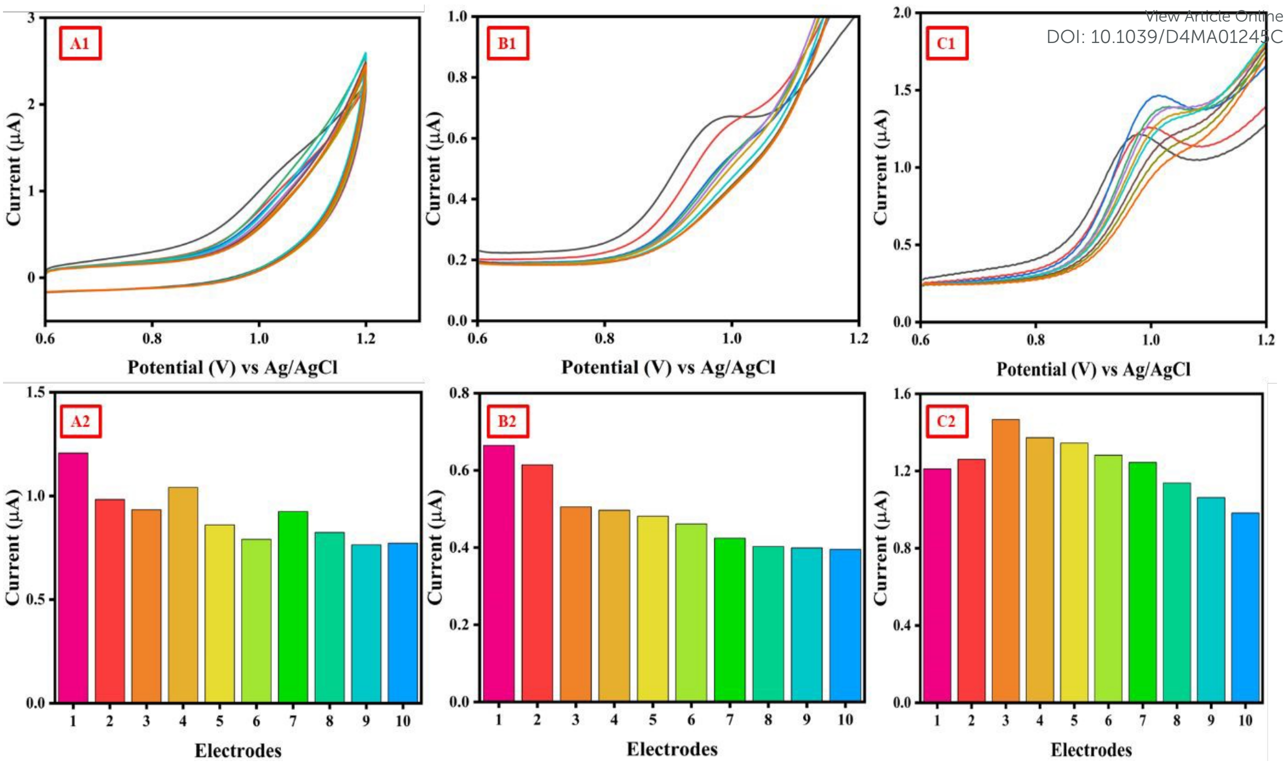

Figure 9. Reproducibility of KTNR fabricated GCEs based on CV (A1-A2), DPV (B1-B2) and SWV (C1-C2) towards efficient sensing of ciprofloxacin.

3.6.8. Selectivity of KTNR/GCE and effect of interfering compounds against ciprofloxacin detection

To ensure selective healthcare monitoring, the KTNR-modified GCE was expected to present a high selectivity for ciprofloxacin against other antibiotics and drugs administered to humans and animals, especially poultry and cattle. To confirm the selectivity of the sensor, the CV was obtained in solutions containing 10 μM of ciprofloxacin (CIP) against same concentration of other antibiotics like enrofloxacin (EF), enrofloxacin (NOR), ofloxacin (OFL) and, Diclofenac (DCF) (**Fig. 10(A)**). In addition to Ciprofloxacin detection, the selectivity of KTNR/GCE was performed using separate 0.1 M phosphate buffer pH=8 containing ciprofloxacin, norfloxacin, ofloxacin and, diclofenac individually. The adsorption capacity and selectivity of the KTNR/GCE for other drug analytes were almost three folds lower compared to ciprofloxacin which showed the highest peak current at a particular 0.98 V potential window, indicating that the binding selectivity of KTNR specific to the ciprofloxacin molecules. The high selectivity can be explained by the unique morphology and high catalytic properties of KTNR. However, the sensor is not at par selective for ciprofloxacin when it was compared with enrofloxacin

View Article Online
DOI: 10.1039/D4MA01245C

which showed twice the amount of current signal within the same potential window. Therefore, the result has provided evidence that KTNR/GCE was selective to other antibiotic classes and drugs but not enrofloxacin due to its similar nature to ciprofloxacin oxidation. Both are zwitterionic molecules that exhibit similar results when tested.

The effect of common inorganic ions, compounds and, drugs existing in various real matrices where ciprofloxacin is detected were also investigated through CV. Compounds like dopamine (DP), uric Acid (UA), urea (UR), ascorbic Acid (AA), glucose (G), and ions, such as Ca^{2+}, Na^{+} , K^{+}, Mg^{2+}, HCO_3^{-} were chosen to test while their concentrations were hundred times higher than that of ciprofloxacin, i.e., by adding 1000 µM of interfering compounds/ions and 10 µM ciprofloxacin in 0.1M phosphate buffer pH = 8, and the results were shown in **Fig. 10(B)**. Also to check the effects of co-exitance of other drugs in real matrices, enrofloxacin, norfloxacin, ofloxacin and diclofenac were taken into consideration in the same manner by checking with 10 µM concentration along with 10 µM ciprofloxacin. The only exception that occurred is in case of enrofloxacin where the interference could be seen to be quite high[37]. Other than that, the response of the sensor towards bare 10 µM ciprofloxacin solution is quite similar to that toward the mixture of ciprofloxacin and interference drugs, compounds and ions, suggesting a very excellent anti-interfering ability of KTNR/GCE even in the micro-environment where the amount of interference may be remarkably higher than ciprofloxacin. The DPV results indicate that the present interfering substances have negligible or no influence on the ciprofloxacin detection in real matrices other than enrofloxacin being present in them. This also owes that the sensor has excellent recognition ability toward the ciprofloxacin detection owing to the unique properties of KTNR.

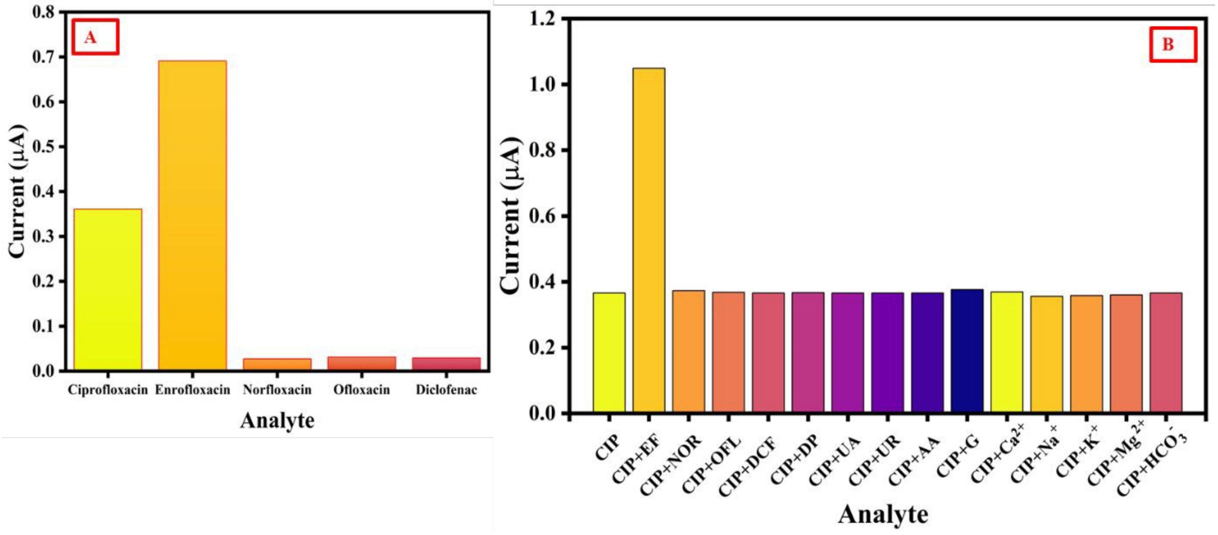

View Article Online
DOI: 10.1039/D4MA01245C

Figure 10. (A) Selectivity of the KTNR/GCE for ciprofloxacin (CIP) against enrofloxacin (EF), norfloxacin (NOR), ofloxacin (OFL), and, diclofenac (DCF); (B) Interference test for electrochemical ciprofloxacin (CIP) a determination under influence of other co-existing compounds like dopamine (DP), uric acid (UA), urea (UR), ascorbic acid (AA), glucose (G), and ions such as Ca^{2+}, Na^{+}, K^{+}, Mg^{2+}, HCO_3^{-}.

3.6.9. Validation of KTNR/GCE for ciprofloxacin detection in complex matrices

The ultrasensitive detection of trace ciprofloxacin in complex matrices existing in animal, environment and human were achieved by the standard addition method. The results are tabulated in **Table 3**. The developed KTNR based ciprofloxacin sensor was successful in detecting the trace analyte concentrations in the tested complex matrices of real samples. Recoveries ranging between 40.13 % to 124 %, are practically viable analytical results for a potential electrochemical sensing device. Spiked samples of milk and ganga water showed low recovery rate indicating the possibility of some interfering compounds being adsorbed or there may be an incident of electro-polymerization of pollutants that causes fouling at the electrode surface which in-turn is hindering the current flow. However, honey, egg and most importantly simulated body fluid (SBF) show excellent recovery rate indicating the efficacy of the proposed sensing device.

Table 3. Electrochemical trace detection of ciprofloxacin spiked in milk, honey and egg, Ganga water, marine water, soil and organic fertilizer samples using KTNR modified electrochemical sensor.

Samples	Spiked (µM)	Detected (µM)	Variance	STD	RSD (%)	Recovery (%)
Milk	0	0	0	0	0	0
	15	6.02	40.3202	6.349819	60.41693	40.13333
Honey	0	0	0	0	0	0
	15	15.3	0.045	0.212132	1.400211	102
Egg	0	0	0	0	0	0
	15	14.6	0.08	0.282843	1.911099	97.33333
Marine Water	0	0	0	0	0	0
	15	6.56	35.6168	5.967981	55.36161	43.73333
Ganga Water	0	0	0	0	0	0
	15	18.6	6.48	2.545584	15.15229	124
Organic Fertilizer	0	0	0	0	0	0
	15	11.4	6.48	2.545584	19.28473	76

View Article Online
DOI: 10.1039/D4MA01245C

Soil	0	0	0	0	0	0
	15	8.3	22.445	4.737615	40.66623	55.33333
SBF	0	0	0	0	0	0
	15	15.1	0.005	0.070711	0.469838	100.6667

4. Conclusion

In conclusion, this research demonstrated the successful synthesis, characterization and fabrication of a novel 2D MXene-derived potassium titanate nanoribbon-based electrochemical sensor for the ultrasensitive detection of ciprofloxacin. The sensor exhibited exemplary performance in all electrochemical voltammetric techniques (CV, DPV, and SWV) achieving a remarkably low LOD and LOQ while being highly selective for other antibiotics and interfering species except enrofloxacin at the particular pH 8. Notably, the sensor demonstrated practical reliability in complex matrices mainly in egg, honey, and SBF, making it a promising candidate for real-world applications in on-site food safety, environmental monitoring, and healthcare diagnostics. Further studies could focus on optimizing sensor stability and exploring miniaturization techniques for technology readiness level (TLR) upgradation and on-site detection to combat antimicrobial resistance against ciprofloxacin, thus contributing to One Health and Sustainable Development Goals.

References

1. LeBel, M. Ciprofloxacin: Chemistry, Mechanism of Action, Resistance, Antimicrobial Spectrum, Pharmacokinetics, Clinical Trials, and Adverse Reactions. *Pharmacotherapy: The Journal of Human Pharmacology and Drug Therapy* **8**, 3–30 (1988).

2. Mason, D. J., Power, E. G. M., Talsania, H., Phillips, I. & Gant, V. A. Antibacterial action of ciprofloxacin. *Antimicrob Agents Chemother* **39**, 2752–2758 (1995).

3. Thomson, C. J. The global epidemiology of resistance to ciprofloxacin and the changing nature of antibiotic resistance: a 10 year perspective. *J Antimicrob Chemother* **43 Suppl A**, 31–40 (1999).

4. Fantin, B. *et al.* Ciprofloxacin dosage and emergence of resistance in human commensal bacteria. *J Infect Dis* **200**, 390 (2009).

5. Herald, C. *et al.* Ciprofloxacin induces apoptosis and inhibits proliferation of human colorectal carcinoma cells. *Br J Cancer* **86**, 443–448 (2002).

6. Peltzer, P. M. *et al.* Ecotoxicity of veterinary enrofloxacin and ciprofloxacin antibiotics on anuran amphibian larvae. *Environ Toxicol Pharmacol* **51**, 114–123 (2017).

7. Hayes, A. *et al.* Predicting selection for antimicrobial resistance in UK wastewater and aquatic environments: Ciprofloxacin poses a significant risk. *Environ Int* **169**, 107488 (2022).

8. Pataki, B. Á. *et al.* Understanding and predicting ciprofloxacin minimum inhibitory concentration in Escherichia coli with machine learning. *Scientific Reports 2020 10:1* **10**, 1–9 (2020).

9. Ewoldt, T. M. J. *et al.* Barriers and facilitators for therapeutic drug monitoring of beta-lactams and ciprofloxacin in the ICU: a nationwide cross-sectional study. *BMC Infect Dis* **22**, (2022).

10. Murray, C. J. *et al.* Global burden of bacterial antimicrobial resistance in 2019: a systematic analysis. *The Lancet* **399**, 629–655 (2022).

11. Mofolorunsho, K. C., Ocheni, H. O., Aminu, R. F., Omatola, C. A. & Olowonibi, O. O. Prevalence and antimicrobial susceptibility of extended-spectrum beta lactamases-producing Escherichia coli and Klebsiella pneumoniae isolated in selected hospitals of Anyigba, Nigeria. *Afr Health Sci* **21**, 505–512 (2021).

12. Githinji, L. J. M., Musey, M. K. & Ankumah, R. O. Evaluation of the fate of ciprofloxacin and amoxicillin in domestic wastewater. *Water Air Soil Pollut* **219**, 191–201 (2011).

13. Liu, H. *et al.* The application of UV/O3 process on ciprofloxacin wastewater containing high salinity: Performance and its degradation mechanism. *Chemosphere* **276**, 130220 (2021).

14. Johansson, C. H., Janmar, L. & Backhaus, T. Toxicity of ciprofloxacin and sulfamethoxazole to marine periphytic algae and bacteria. *Aquat Toxicol* **156**, 248–258 (2014).

15. de Souza, C. C., Alves, G. F., Lisboa, T. P., Matos, M. A. C. & Matos, R. C. Low-cost paper-based electrochemical sensor for the detection of ciprofloxacin in honey and milk samples. *Journal of Food Composition and Analysis* **112**, (2022).

16. Onken, A. *et al.* Predominance of multidrug-resistant Salmonella Typhi genotype 4.3.1 with low-level ciprofloxacin resistance in Zanzibar. *PLoS Negl Trop Dis* **18**, e0012132 (2024).

17. Wu, B. *et al.* Facile synthesis of dendritic-like CeO2/rGO composite and application for detection of uric acid and tryptophan simultaneously. *J Solid State Chem* **296**, 122023 (2021).

18. Zhang, S., Ling, P., Chen, Y., Liu, J. & Yang, C. 2D/2D porous Co3O4/rGO nanosheets act as an electrochemical sensor for voltammetric tryptophan detection. *Diam Relat Mater* **135**, 109811 (2023).

19. Li, G. *et al.* Highly stable electrochemical sensing platform for the selective determination of pefloxacin in food samples based on a molecularly imprinted-polymer-coated gold nanoparticle/black phosphorus nanocomposite. *Food Chem* **436**, 137753 (2024).

20. Xie, L. *et al.* An efficient voltammetric sensing platform for trace determination of Norfloxacin based on nanoplate-like α-zirconium phosphate/carboxylated multiwalled carbon nanotube nanocomposites. *Microchemical Journal* **206**, 111451 (2024).

21. Wan, X. *et al.* UiO-66/Carboxylated Multiwalled Carbon Nanotube Composites for Highly Efficient and Stable Voltammetric Sensors for Gatifloxacin. *ACS Appl Nano Mater* **6**, 19403–19413 (2023).

22. Li, G. *et al.* Lamellar α-Zirconium Phosphate Nanoparticles Supported on N-Doped Graphene Nanosheets as Electrocatalysts for the Detection of Levofloxacin. *ACS Appl Nano Mater* **6**, 17040–17052 (2023).

23. Li, G. *et al.* Molecularly imprinted polypyrrole film-coated poly(3,4-ethylenedioxythiophene):polystyrene sulfonate-functionalized black phosphorene for the selective and robust detection of norfloxacin. *Mater Today Chem* **26**, 101043 (2022).

24. Mathai, T., Pal, T., Prakash, N. & Mukherji, S. Portable biosensor for the detection of Enrofloxacin and Ciprofloxacin antibiotic residues in food, body fluids, environmental and wastewater samples. *Biosens Bioelectron* **237**, 115478 (2023).

25. Appu Mini, A. & Raghavan, V. Mxene-derived Na2O7Ti3 nanoribbon as a promising electrode material for the detection of ethyl paraoxon in complex matrices. *Microchemical Journal* **201**, 110674 (2024).

26. Dong, Y. *et al.* Ti3C2 MXene-Derived Sodium/Potassium Titanate Nanoribbons for High-Performance Sodium/Potassium Ion Batteries with Enhanced Capacities. *ACS Nano* **11**, 4792–4800 (2017).

27. Zheng, F., Ma, F., Cai, L. & Zhang, X. Proton conduction enabled highly selective acetonitrile detection at moderate operating temperature by using Ag-decorated sodium titanate nanoribbons. *J Mol Liq* **395**, 123843 (2024).

28. Alves, D. C. B. *et al.* Hydrogen sensing in titanate nanotubes associated with modulation in protonic conduction. *Nanotechnology* **22**, (2011).

29. Zhang, Y. *et al.* Excessive use of enrofloxacin leads to growth inhibition of juvenile giant freshwater prawn Macrobrachium rosenbergii. *Ecotoxicol Environ Saf* **169**, 344–352 (2019).

30. Cai, L. & Zhang, X. Sodium titanate: A proton conduction material for ppb-level NO2 detection with near-zero power consumption. *J Hazard Mater* **462**, (2024).

31. Mestres, C., Alsina, M. A., Busquets, M. A., Haro, I. & Reig, F. Interaction of Enrofloxacin with Phospholipid Mono-and Bilayers. *Langmuir* **10**, 767–772 (1994).

32. Liu, W. *et al.* Inhibition of microbial growth on air cathodes of single chamber microbial fuel cells by incorporating enrofloxacin into the catalyst layer. *Biosens Bioelectron* **72**, 44–50 (2015).

33. Windust, A. *et al.* High polarity analytes in food - enrofloxacin and sulfadiazine in bovine tissue (CCQM-K141). *Metrologia* **56**, 08005 (2019).

34. Gaussian 09 Citation | Gaussian.com. https://gaussian.com/g09citation/.

35. Thukkaram, M. P. *et al.* Titanium carbide MXene and V2O5 composite-based electrochemical sensor for detection of bisphenol A. *Microchemical Journal* **193**, (2023).

36. Mini, A. A. *et al.* CuO nanoparticles passivated 2D MXene-based voltammetric sensor for detecting environmental hazardous pollutant. *Microchemical Journal* **201**, 110648 (2024).

37. Chakravorty, A. & Raghavan, V. Proton conductive 2D MXene-derived potassium titanate nanoribbons fabricated electrochemical platform for trace detection of enrofloxacin. *Chemosphere* **366**, 143520 (2024).

38. Wang, S. *et al.* Molten salt synthesis of MXene-derived hierarchical titanate for effective strontium removal. *J Hazard Mater* **469**, 134079 (2024).

39. Dong, Y. *et al.* Ti3C2 MXene-Derived Sodium/Potassium Titanate Nanoribbons for High-Performance Sodium/Potassium Ion Batteries with Enhanced Capacities. *ACS Nano* **11**, 4792–4800 (2017).

40. Awasthi, S., Pandey, S. K., Gaur, J. K. & Srivastava, C. Load-bearing study and interfacial interactions of hydroxyapatite composite coatings for bone tissue engineering. *Mater Chem Front* **6**, 3731–3747 (2022).

41. Awasthi, S., Gaur, J. K., Pandey, S. K., Bobji, M. S. & Srivastava, C. High-Strength, Strongly Bonded Nanocomposite Hydrogels for Cartilage Repair. *ACS Appl Mater Interfaces* **13**, 24505–24523 (2021).

42. Singh, K. *et al.* Interpretation of Adsorption Behavior of Carboxymethyl Cellulose onto Functionalized Accurel Polymeric Surface. *Ind Eng Chem Res* **59**, 19102–19116 (2020).

43. Pandey, S. K. Novel and Polynuclear K- And Na-Based Superalkali Hydroxides as Superbases Better Than Li-Related Species and Their Enhanced Properties: An Ab Initio Exploration. *ACS Omega* **6**, 31077–31092 (2021).

44. Lele, N., Bambo, M. F., Mmutlane, E. M. & Dlamini, L. N. Construction of a multifunctional MXene@β-cyclodextrin nanocomposite with photocatalytic properties. *Emergent Mater* **6**, 605–626 (2023).

45. Catti, M., Pinus, I. & Scherillo, A. On the crystal energy and structure of A2TinO2n+1 (A=Li, Na, K) titanates by DFT calculations and neutron diffraction. *J Solid State Chem* **205**, 64–70 (2013).

46. Anasori, B., Lukatskaya, M. R. & Gogotsi, Y. 2D metal carbides and nitrides (MXenes) for energy storage. *Nature Reviews Materials 2017 2:2* **2**, 1–17 (2017).

47. Li, L. *et al.* Surface and Interface Engineering of Nanoarrays toward Advanced Electrodes and Electrochemical Energy Storage Devices. *Advanced Materials* **33**, 2004959 (2021).

48. Zargar, S. A. *et al.* Synthesis of novel 2D/2D Ti3C2Tx MXene / 1T-MoS2 heterostructure enhanced with carbon nanotubes as a highly-efficient electrode for hybrid capacitive deionization. *J Alloys Compd* **981**, 173765 (2024).

49. Wang, D., Zhu, Z., He, B., Ge, Y. & Zhu, D. Effect of the breakdown time of a passive film on the electrochemical machining of rotating cylindrical electrode in NaNO3 solution. *J Mater Process Technol* **239**, 251–257 (2017).

50. Sun, W. *et al.* Cathodic membrane–based electrochemical redox process for water treatment: a review. *Curr Opin Chem Eng* **44**, 101023 (2024).

51. Sun, Y., Gao, S., Lei, F. & Xie, Y. Atomically-thin two-dimensional sheets for understanding active sites in catalysis. *Chem Soc Rev* **44**, 623–636 (2015).

52. Jiang, P. *et al.* A Cost-Effective 3D Hydrogen Evolution Cathode with High Catalytic Activity: FeP Nanowire Array as the Active Phase. *Angewandte Chemie* **126**, 13069–13073 (2014).

53. Costentin, C., Robert, M. & Savéant, J. M. Catalysis of the electrochemical reduction of carbon dioxide. *Chem Soc Rev* **42**, 2423–2436 (2013).

54. Tatara, R. *et al.* The Effect of Electrode-Electrolyte Interface on the Electrochemical Impedance Spectra for Positive Electrode in Li-Ion Battery. *J Electrochem Soc* **166**, A5090–A5098 (2019).

55. Tsao, H. N. *et al.* Influence of the interfacial charge-transfer resistance at the counter electrode in dye-sensitized solar cells employing cobalt redox shuttles. *Energy Environ Sci* **4**, 4921–4924 (2011).

56. Watanabe, H., Sugiura, Y., Shitanda, I. & Itagaki, M. Faradaic impedance and discharge reactions in lithium sulfur battery with sparingly solvating electrolyte. *Electrochim Acta* **477**, 143759 (2024).

57. Sutar, S. D., Patil, I., Parse, H., Mukherjee, P. & Swami, A. Ti3C2Tx/TiO2@GO* Heterostructure: A Strategy to Design High-Specific Capacitive Electrodes for a Solid-State Supercapacitor. *ACS Appl Energy Mater* (2024) doi:10.1021/ACSAEM.4C00210.

58. Ibrahim, H. & Temerk, Y. Surface decoration of functionalized carbon black nanoparticles with nanosized gold particles for electrochemical sensing of diuretic spironolactone in patient plasma. *Microchemical Journal* **178**, 107425 (2022).

59. Sun, J. *et al.* Determination of lipophilicity of two quinolone antibacterials, ciprofloxacin and grepafloxacin, in the protonation equilibrium. *European Journal of Pharmaceutics and Biopharmaceutics* **54**, 51–58 (2002).

60. Becker, P. M., Heinze, K., Sarkar, B. & Kästner, J. Redox−Acid/Base Phase Diagrams as an Entry to Computational Redox Chemistry. *ChemElectroChem* **11**, e202400301 (2024).

61. Elancheziyan, M., Singh, M. & Won, K. Gold Nanoparticle-Embedded Thiol-Functionalized Ti3C2Tx MXene for Sensitive Electrochemical Sensing of Ciprofloxacin. *Nanomaterials* **14**, 1655 (2024).

62. Bhuvaneswari, C. & Ganesh Babu, S. Review of 2-D support-based nanocomposites for electrocatalytic detection of pharmaceutical drugs. *Journal of Materials Science 2024 59:26* **59**, 11687–11717 (2024).

63. Tonelli, D., Gualandi, I., Scavetta, E. & Mariani, F. Focus Review on Nanomaterial-Based Electrochemical Sensing of Glucose for Health Applications. *Nanomaterials 2023, Vol. 13, Page 1883* **13**, 1883 (2023).

64. Blumberger, J., Bernasconi, L., Tavernelli, I., Vuilleumier, R. & Sprik, M. Electronic Structure and Solvation of Copper and Silver Ions: A Theoretical Picture of a Model Aqueous Redox Reaction. *J Am Chem Soc* **126**, 3928–3938 (2004).

65. Tamura, H. Theorization on ion-exchange equilibria: activity of species in 2-D phases. *J Colloid Interface Sci* **279**, 1–22 (2004).

66. de Sá, M. H. & Pereira, C. M. The relevance of the initial conditions in glassy carbon electrode sensing applications: the ferri/ferrocyanide redox reaction model system in aqueous solution. *Electrochim Acta* **489**, 144158 (2024).

67. Yu, Z. *et al.* Electrolyte engineering for efficient and stable vanadium redox flow batteries. *Energy Storage Mater* **69**, 103404 (2024).

68. Pati, J. & Dhaka, R. S. Mixed polyanionic NaFe1.6V0.4(PO4)(SO4)2@CNT cathode for sodium-ion batteries: Electrochemical diffusion kinetics and distribution of relaxation time analysis at different temperatures. *J Power Sources* **609**, 234646 (2024).

69. Zhu, P. & Zhao, Y. Effects of electrochemical reaction and surface morphology on electroactive surface area of porous copper manufactured by Lost Carbonate Sintering. *RSC Adv* **7**, 26392–26400 (2017).

70. Gómez, R. & Clavilier, J. Electrochemical behaviour of platinum surfaces containing (110) sites and the problem of the third oxidation peak. *Journal of Electroanalytical Chemistry* **354**, 189–208 (1993).

71. Grdeń, M., Łukaszewski, M., Jerkiewicz, G. & Czerwiński, A. Electrochemical behaviour of palladium electrode: Oxidation, electrodissolution and ionic adsorption. *Electrochim Acta* **53**, 7583–7598 (2008).

72. Wipf, D. O., Kristensen, E. W., Deakin, M. R. & Wightman, R. M. Fast-Scan Cyclic Voltammetry as a Method to Measure Rapid, Heterogeneous Electron-Transfer Kinetics. *Anal Chem* **60**, 306–310 (1988).

73. Ruiz, Y. *et al.* Repeatability of low scan rate cyclic voltammetry in bioelectrochemical systems and effects on their performance. *Journal of Chemical Technology and Biotechnology* **95**, 1533–1541 (2020).

74. Anantharaj, S. & Noda, S. iR drop correction in electrocatalysis: everything one needs to know! *J Mater Chem A Mater* **10**, 9348–9354 (2022).

75. Yahyapour, M., Ranjbar, M. & Mohadesi, A. Determination of ciprofloxacin drug with molecularly imprinted polymer/co- metal organic framework nanofiber on modified glassy carbon electrode (GCE). *Journal of Materials Science: Materials in Electronics* **32**, 3180–3190 (2021).

76. Pan, M., Guo, P., Liu, H., Lu, J. & Xie, Q. Graphene oxide modified screen-printed electrode for highly sensitive and selective electrochemical detection of ciprofloxacin residues in milk. *J Anal Sci Technol* **12**, 1–7 (2021).

77. Zhao, J., Huang, P. & Jin, W. Electrochemical sensor based on TiO2/polyvinyl alcohol nanocomposite for detection of ciprofloxacin in rainwater. *Int J Electrochem Sci* **16**, 211018 (2021).

78. Jain, P. & Motghare, R. V. Electro-Oxidation and Determination of Ciprofloxacin at f-MWCNT@Poly-Aniline Glassy Carbon Electrode. *J Electrochem Soc* **169**, 056515 (2022).

79. Chaabani, A., Ben Jabrallah, T. & Belhadj Tahar, N. Electrochemical Oxidation of Ciprofloxacin on COOH-Functionalized Multi-Walled Carbon Nanotube–Coated Vitreous Carbon Electrode. *Electrocatalysis* **13**, 402–413 (2022).

80. Muungani, G., Moodley, V. & van Zyl, W. E. Solid-state synthesis of the phyllosilicate Effenbergerite (BaCuSi4O10) for electrochemical sensing of ciprofloxacin antibiotic in pharmaceutical drug formulation. *J Appl Electrochem* **52**, 285–297 (2022).

81. Pham, T. S. H. *et al.* Graphene Nanocomposites Based Electrochemical Sensing Platform for Simultaneous Detection of Multi-drugs. *Electroanalysis* **34**, 435–444 (2022).

View Article Online
DOI: 10.1039/D4MA01245C

82. Faria, L. V. *et al.* Square-Wave Voltammetry Determination of Ciprofloxacin in Pharmaceutical Formulations and Milk Using a Reduced Graphene Oxide Sensor. *J Braz Chem Soc* **30**, 1947–1954 (2019).

83. Surya, S. G. *et al.* A chitosan gold nanoparticles molecularly imprinted polymer based ciprofloxacin sensor. *RSC Adv* **10**, 12823–12832 (2020).

84. Kumar, S., Karfa, P., Majhi, K. C. & Madhuri, R. Photocatalytic, fluorescent BiPO4@Graphene oxide based magnetic molecularly imprinted polymer for detection, removal and degradation of ciprofloxacin. *Materials Science and Engineering: C* **111**, 110777 (2020).

85. Vedhavathi, H. S., Sanjay, B. P., Basavaraju, M., Madhukar, B. S. & Kumara Swamy, N. Development of ciprofloxacin sensor using iron-doped graphitic carbon nitride as transducer matrix: Analysis of ciprofloxacin in blood samples: Original scientific paper. *Journal of Electrochemical Science and Engineering* **12**, 59–70 (2022).

86. Adane, W. D., Chandravanshi, B. S. & Tessema, M. A simple, ultrasensitive and cost-effective electrochemical sensor for the determination of ciprofloxacin in various types of samples. *Sens Biosensing Res* **39**, 100547 (2023).

View Article Online
DOI: 10.1039/D4MA01245C

Data Availability Statement

From,
Dr. Vimala Raghavan
Associate Professor
Centre for Nanotechnology Research
Vellore Institute of Technology, Vellore
Tamil Nadu, India - 632014
Corresponding author Email Id- vimala.r@vit.ac.in

Dr. Sarvesh K. Pandey
Assistant Professor
Department of Chemistry, Maulana Azad National Institute of Technology Bhopal, Bhopal – 462003, Madhya Pradesh, India
Co-corresponding author email ID: sarvesh@manit.ac.in

To,
The Editor-in-Chief
Journal of Materials Chemistry B (JMC B)

The data will be made available on request.

With Kind regards

Dr. Vimala Raghavan

Dr. Sarvesh K. Pandey